TUNL REU III

RESEARCH REPORT

30 MAY 2017 – 5 AUGUST 2017

Triangle Universities Nuclear Laboratory

Duke University
North Carolina State University
University of North Carolina at Chapel Hill

Box 90308, Durham, North Carolina 27708-0308, USA

The research described in this report is supported by the United States Department of Energy, Office of Science (Low Energy Nuclear Physics and Medium Energy Nuclear Physics Programs), under:

Grant No. DE-FG02-97ER41033 (Duke University),
Grant No. DE-FG02-97ER41042 (North Carolina State University), and
Grant No. DE-FG02-97ER41041 (University of North Carolina).

The TUNL Research Experiences for Undergraduates (REU) Program is supported by the National Science Foundation under:

Grant No. NSF-PHY-1461204.

Contents

Introduction

An important national goal is to develop a diverse, internationally competitive, and globally engaged workforce in science and engineering. The Research Experiences for Undergraduates (REU) program is part of the effort to achieve that goal. The REU program at the Triangle Universities Nuclear Laboratory (TUNL) and Duke University provides a ten-week opportunity for undergraduate students to pursue research in the areas of nuclear and particle physics. This allows promising physics majors to broaden their education through participation in research at the frontiers of these exciting scientific fields.

In 2017, fifteen students participated in the TUNL REU Program: eleven spent the summer working on nuclear physics projects on the Duke campus, while the other four spent four weeks at Duke and six weeks at the European Center for Nuclear Research (CERN) near Geneva, Switzerland, working on particle physics projects. Having the nuclear and particle physics students in the same program facilitated cross-field intellectual exchange and the sharing of resources needed by both groups, while the participation of the Duke high energy physics group in the program gives it an international component.

Through introductory lectures and direct research involvement, the students gain experience and insights in the main stages of scientific research in nuclear and particle physics:

- The development of concepts to probe specific features of nuclear matter, particles and fields;
- The design, construction, testing, and installation of equipment and instrumentation;
- Data acquisition, analysis, and interpretation; and
- The dissemination of research results.

In addition to direct involvement in research projects, the REU program at Duke includes activities that are designed to broaden the students' physics foundation, enhance their research skills, and build confidence. These activities include: (1) regular meetings with the program coordinator, (2) research tutorials and special topic lectures, (3) a science writing tutorial, and (4) a required report and presentation by each student at the end of the program. The research reports written by the students form the main body of this document.

Personnel

2017 TUNL REU Participants

Student	*Home Institution*	*Faculty Advisor*	*Class*
Chad Barrow	North Carolina State University	Paul Huffman	Jr
Samuel Belling	University of Wisconsin Platteville	Phil Barbeau	Jr
Taylor Contreras	University of Oregon	Al Goshaw	Jr
Keilah Davis	North Carolina State University	Richard Longland	So
Marcos Flores	New Mexico Institute of Mining and Technology	Ayana Arce	Jr
Shalane Hairston	North Carolina Central University	Diane Markoff	Jr
Elise Le Boulicaut	Gustavus Adolphus College	Mark Kruse	Jr
Alleta Maier	Linfield College	Phil Barbeau	Jr
Michael Narijauskas	Central Connecticut State University	John Kelley	Jr
Cynthia Nunez	Florida International University	Kate Scholberg	Jr
James Parkes	University of Alabama	John Wilkerson	Jr
Andrew Tillett	University of North Carolina at Chapel Hill	Christian Iliadis	Jr
Nathan Villiger	Butler University	Calvin Howell	Jr
Elizabeth Wildenhain	University of Notre Dame	Krishichayan	Jr

2017 TUNL REU Administration

Principal Investigator:
Professor Calvin R. Howell

Co-Principal Investigator:
Professor Ayana Arce

Program Coordinator:
Dr. Alexander Crowell

Participants in the TUNL Research Experiences for Undergraduates (REU) program are shown on the Duke campus. Shown in the photograph from left to right are: (front row) Shalane Hairston (North Carolina Central University), Taylor Contreras (University of Oregon), Cynthia Nunez (Florida International University), Keilah Davis (North Carolina State University), Alleta Maier (Linfield College), Elizabeth Wildenhain (University of Notre Dame), Elise Le Boulicaut (Gustavus Adolphus College); (back row) Nathan Villiger (Butler University), Samuel Belling (University of Wisconsin Platteville), James Parkes (University of Alabama), Marcos Flores (New Mexico Institute of Mining and Technology), Michael Narijauskas (Central Connecticut State University), Andrew Tillett (University of North Carolina at Chapel Hill), Chad Barrow (North Carolina State University), Riley Xu (Carnegie Mellon University).

Research Based at Duke

Chapter 1

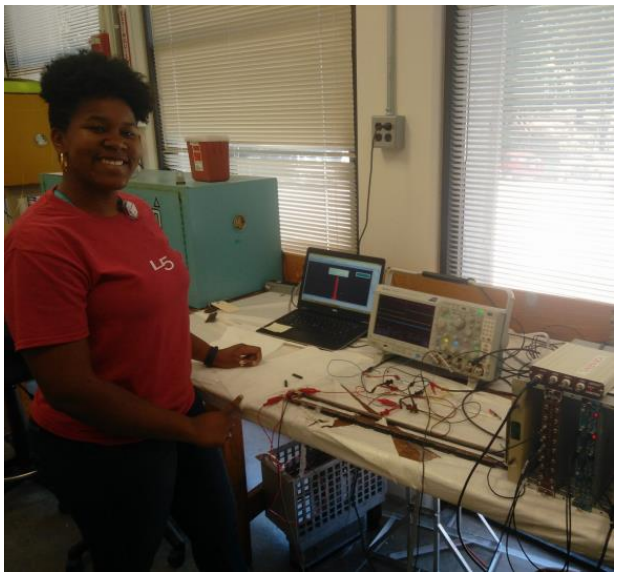

1.1 Using Proton Transfer Reactions to Constrain Stellar Reaction Cross Sections

K.S. Davis, *North Carolina State University, Raleigh, NC*; R. Longland, K. Setoodehnia, C. Marshall, F. Portillo, *TUNL*

The proton transfer in ^{22}Ne(^{3}He,d)^{23}Na can be used to determine the reaction rate of proton capture in ^{22}Ne(p,γ)^{23}Na. Measuring the transferred angular momentum, or spin, of ^{23}Na is crucial to determining this rate. We measured the ^{22}Ne(^{3}He,d)^{23}Na cross section at 8 angles. Our result for the transferred angular momentum in the E_x = 8945 keV excited state of ^{23}Ne appears to agree with an earlier indirect measurement while disagreeing with direct measurements and theoretical predictions.

The ^{22}Ne(p,γ)^{23}Na reaction may have a significant effect on the surface abundance of sodium in AGB stars. The rate of this reaction is calculated using the cross section of the ^{22}Ne(p,γ)^{23}Na reaction and the energy distribution of particles in a stellar plasma. However, the cross section of this reaction is quite small, thus we use the proton transfer of ^{22}Ne(^{3}He,d)^{23}Na to indirectly test the former reaction. Our work probes the E_x = 8945 keV excited state of the resulting ^{23}Na.

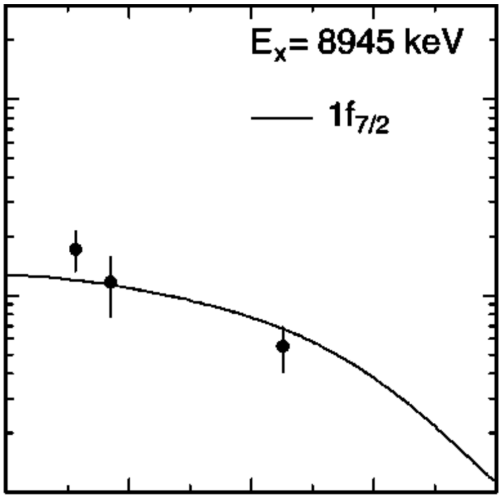

Figure 1.1: Differential cross section (mb/sr) vs. $\theta_{c.m.}$ (deg). Fit to the ^{22}Ne(^{3}He,d)^{23}Na data from Ref. [Hal01] corresponding to an L = 3 angular momentum transfer in the E_x=8945 keV state of ^{22}Ne.

A previous study of this excited state concluded that the angular momentum transfer corresponded to $L = 3$ and $J^\pi = 7/2^-$ [Hal01]. This result, shown in Fig. 1.1, disagreed with theoretical predictions and direct measurements that stated the angular momentum transfer was $L = 2$ with $J^\pi = 3/2^+$ [Kel17]. We replicated and improved the aforementioned study by collecting data with lower statistical uncertainty at more angles.

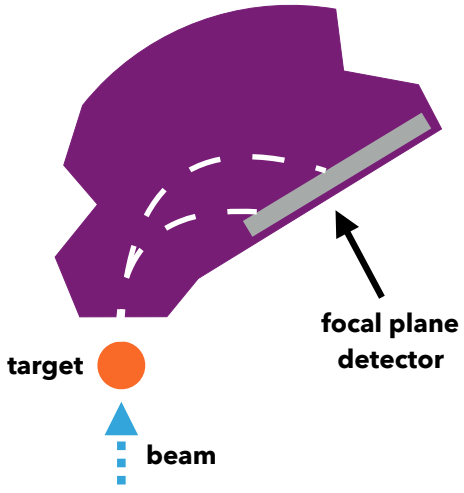

Figure 1.2: Overhead view of experimental setup (not to scale).

The FN tandem accelerator at TUNL provided a ^{3}He^{2+} beam at 20 MeV during a 72-hour run. The outgoing deuterons were analyzed with the Enge Split-Pole Magnet and focal plane detector with the magnetic field set at 1.08 T (see Fig. 1.2). We col-

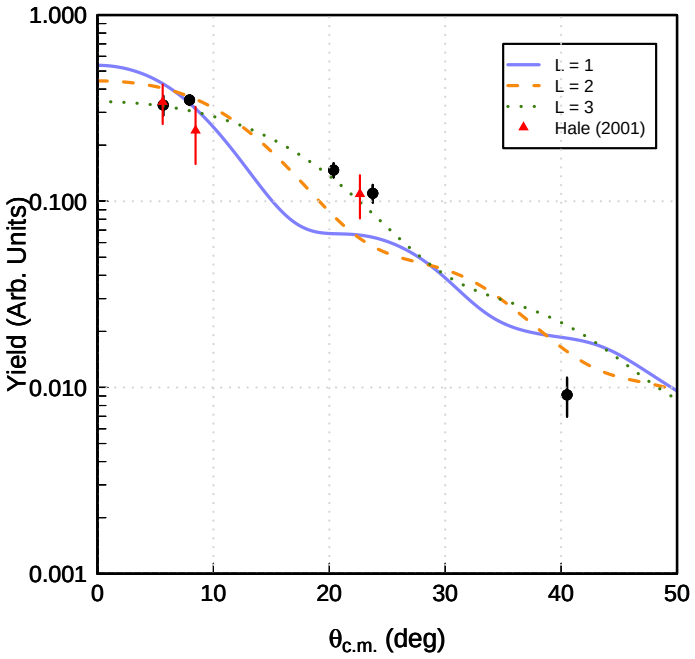

Figure 1.3: Theoretical cross sections for ^{22}Ne(^{3}He,d)^{23}Na. The variable L represents the transferred angular momentum. The black (circle) points represent our data and the red (triangle) points represent previous work [Hal01].

lected data at 8 lab angles. The ^{22}Ne targets were implanted on carbon foils at the University of North Carolina at Chapel Hill.

Initial elastic scattering confirmed a sufficient amount of ^{22}Ne in the target. Measurements with carbon targets were also made to account for any background from the carbon foils on which the ^{22}Ne was implanted. Although we collected data at 8 different angles, only at 5 angles was the background distinguishable from our data. The E_x=8945 keV peak was identified in the spectra of deuteron counts at each of these angles. We then calculated the ^{22}Ne yield from the area under these peaks.

The relative yields are plotted in Fig. 1.3 using the state-of-the-art reaction code, FRESCO to generate three theoretical cross section curves for angular momentum transfers of $L = 1, 2,$ and 3 respectively using previous optical-model parameters [Hal01]. In addition to taking data at more angles, our longer run time and higher beam current provided us with better statistics than the previous measurement. From visual confirmation and chi-square tests, our initial conclusion is that the angular momentum transfer corresponds to $L = 3$ and $J^{\pi} = 7/2^{-}$.

Our results further confirm the ambiguity between direct and indirect measurements of the ^{22}Ne$(p,\gamma)^{23}$Na cross section. The effect of this measurement on the reaction rate is roughly a factor of 30, which our calculations indicate will correspond to a factor of 13 decrease in the production of ^{23}Na in AGB stars. However, our results depend on a single set of model parameters, which may not properly describe the reaction system.

Future work will include a systematic study of model effects on our angular momentum determination.

[Hal01] S. E. Hale *et al.*, Phys. Rev. C, **65**, 015801 (2001).

[Kel17] K. J. Kelly *et al.*, Phys. Rev. C, **95**, 015806 (2017).

1.2 Measurement of the ^{191,193}Ir(n,2n)^{190,192}Ir Reaction Cross Section Between 9.0 and 16.5 MeV

E.R. Wildenhain, *University of Notre Dame, South Bend, IN*; S.W. Finch, W. Tornow, Krishichayan, *TUNL*

Iridium is one of the elements prioritized by nonproliferation and homeland security agencies. In addition, ^{192}Ir is being used in various medical treatments. Improved data and corresponding evaluations of neutron-induced reactions on the iridium isotopes are required to meet the demands of several applications of societal interest. This study measured the cross section of the ^{191,193}Ir$(n, 2n)^{190,192}$Ir reactions at energies from 9.0 to 16.5 MeV using the activation technique. Measured cross-section data are compared to previous data and to predictions from nuclear data libraries (e.g. ENDF).

Measuring reaction cross sections allows for discrimination between nuclear models and for use of the reaction in practical applications. Iridium is an element prioritized by nonproliferation and homeland security agencies, and the $(n, 2n)$ reaction with naturally occurring iridium isotopes has various applications in medical treatment [Cow07] and as a material for the construction of activation detectors [Tal07]. These applications of the $(n, 2n)$ reaction require systematic and precise measurements of the reaction cross section. In literature, the ^{191,193}Ir$(n, 2n)$ cross section has been measured since 1975 but only concentrated at or higher than E_n = 14.8 MeV [Bay75]. The present measurements in this study provide a systematic and self-consistent method to calculate the ^{191,193}Ir$(n, 2n)$ cross section from threshold to 16.5 MeV energy regime.

The experiments were performed using the 10 MV model FN tandem accelerator at TUNL via the neutron activation method [Bhi14, Rei02]. Monoenergetic neutrons for irradiations at 9.0, 10.0, 11.0, and 12.0 MeV were produced using the ^{2}H$(d, n)^3$He reaction by bombarding deuterium gas with a deuteron beam. For irradiations at 14.8 and 16.5 MeV, monoenergetic neutrons were produced using the ^{3}H$(d, n)^4$He reaction. The target for each irradiation consisted of a natural high purity iridium foil (37.3% ^{191}Ir and 62.7% ^{193}Ir) with a 11.1-mm diameter and 0.125-mm thickness sandwiched between two ^{197}Au monitor foils of 0.05-mm thickness. The incident neutron flux was obtained from the monitor reaction on ^{197}Au. The required cross-section values for the ^{197}Au$(n, 2n)^{196}$Au reaction were taken from the work of Zolotarev [Zol09].

Following activation, the Ir and Au monitor foils were γ-ray counted at TUNL's low-background counting facility using high-efficient (60% relative efficiency) HPGe detectors. Offline γ-ray analysis was done using the TV software. From the cycled decay activities, decay curves were generated for ^{190m2}Ir, ^{190}Ir, and ^{196}Au. The corresponding calculated half-lives are in good agreement with the literature values.

From the activity measurements, the cross sections for the ^{191}Ir$(n, 2n)^{190}$Ir, ^{191}Ir$(n, 2n)^{190m2}$Ir, and ^{193}Ir$(n, 2n)^{192}$Ir reactions were calculated using the following equation (see Ref. [Rei02] for the variable definitions):

$$\sigma_{Ir} = \sigma_{Au}\left(\frac{F_{Ir}}{F_{Au}}\right) \tag{1.1}$$

where F_{Ir} and F_{Au} represent the molar reaction rates of Ir and Au respectively.

The measured cross sections are plotted in Figs. 1.4 through 1.6 along with previous literature values and evaluations. In Fig. 1.4 we see that our cross-section values for the production of ^{190m2}Ir agree with previous measurements. The values from this study tend to be slightly higher than the predicted values from the ENDF/B-VII.1 evaluation. In Fig. 1.5, the cross sections for the sum of ^{190}Ir ground state and first metastable state (g + m1) agree with the lower cluster of data around 15 MeV from studies by Filatenkov [Fil16] and Konno [Kon93] rather than the higher data from studies done by Herman [Her84]. The evaluation curve from ENDF/B-VII.1 corresponds best with the higher data points. However, the evaluation calculation is a sum of cross sections from all isomeric states. Because the cross section from ^{190m2}Ir is significant, the g + m1 cross sec-

tion ought to be lower than the evaluation curve.

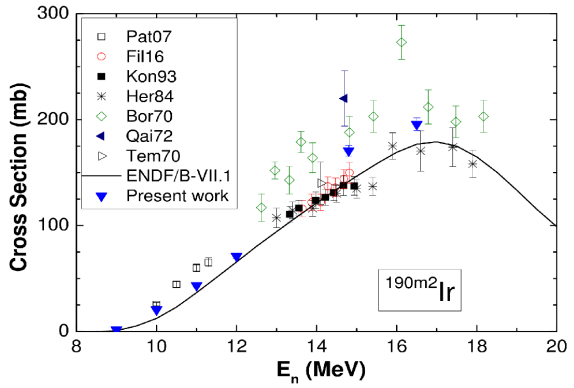

Figure 1.4: Measured cross section for the production of ^{190m2}Ir compared to literature values and the evaluation cross section curve from ENDF/B-VII.1.

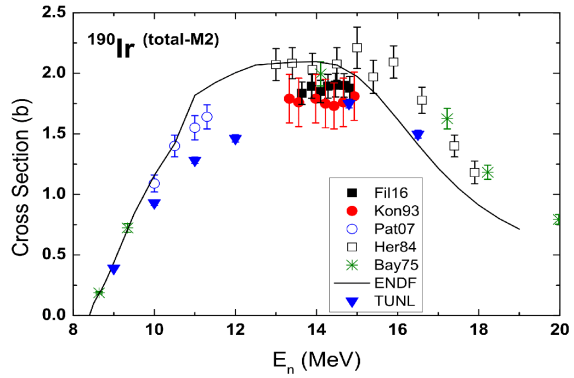

Figure 1.5: Measurements for the difference between the total ^{190}Ir cross section and the ^{190m2}Ir cross section compared to literature values and evaluation cross section curves. Evaluation curves are for the total cross section.

As seen in Fig. 1.6, the cross section values for ^{192}Ir agree with previous findings and fill in a number of holes in the literature. The measurements at 9.0, 10.0, 11.0, and 12.0 are the first at these energies. The evaluation curves from TENDL-14 and JEFF-3.2 match these data better than the curve from ENDF/B-VII.1, especially in the 10.0-12.0 MeV range.

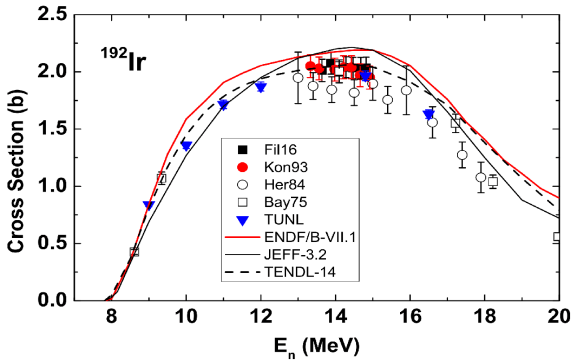

Figure 1.6: Measured cross section for the production of ^{192}Ir compared to literature values and evaluation cross-section curves.

In the future, we plan to take data at E_n = 13.0 and 14.0 MeV. Given the longer half-life of ^{192}Ir (73.83 d), the previously irradiated Ir samples will also be counted for a longer period in order to generate the decay curves for ^{192}Ir.

[Bay75] B. P. Bayhurst *et al.*, Phys. Rev. C, **12**, 451 (1975).

[Bhi14] M. Bhike and W. Tornow, Phys. Rev. C, **89** (2014).

[Cow07] S. Cowell *et al.*, International Conference on Nuclear Data for Science and Technology, (2007).

[Fil16] A. A. Filatenkov, *Neutron activation cross sections measured at KRI in neutron energy region 13.4 - 14.9 MeV*, Technical Report 0460, 2016, USSR report to the I.N.D.C.

[Her84] M. Herman, A. Marcinkowski, and K. Stankiewicz, Nucl. Phys. A, **430**, 69 (1984).

[Kon93] C. Konno *et al.*, Technical Report 1329, 1993, JAERI Reports.

[Rei02] P. Reimer, Ph.D. thesis, Institut für Nuklearchemie, 2002.

[Tal07] P. Talou *et al.*, *Nuclear Weapons Highlights*, Technical Report LALP-07-041, Los Alamos National Laboratory, 2007.

[Zol09] K. I. Zolotarev, Technical report, International Atomic Energy Agency, Vienna, Austria, 2009.

1.3 Developing a Neutron Beam Imaging System

N.J. Villiger, *Butler University, Indianapolis, IN*; C.R. Howell, F.Q. Friesen, J.A. Runge, *TUNL*

The use of neutron beams in experiments requires precise knowledge of the cross-sectional beam profile and the beam axis direction. In the past, experimenters at TUNL made these types of measurements by scanning a detector horizontally and vertically across the beam at two locations along its path. Recently, it was demonstrated by Zhang [Zha17] that position sensitive photomultiplier tubes coupled with BGO scintillators could allow measurements to be completed much faster. Unfortunately, BGO is highly sensitive to γ rays. Therefore, we expanded Zhang's concept by using the distinct timing signatures of γ rays and neutrons to discriminate between the two types of events. Our system can be used to quickly and accurately characterize the cross-sectional profile and beam axis of a neutron beam, which allows experimenters to optimize their experimental setup and beam time.

The shielded neutron source (SNS) at TUNL is capable of providing a well-collimated and nearly monoenergetic beam of neutrons. Researchers at TUNL can utiliize the SNS to perform precise experiments with neutron beams or create specific nuclides via activation to then use elsewhere. In order to optimize their experiments, it is important to know the cross-sectional profile and axis direction of the neutron beam. After leaving the collimator the beam diverges linearly, which allows researchers to position their target to take maximum advantage of the size of the beam. A complicating factor, though, is the fact that the beam axis is not necessarily the same as the optical axis. For this reason, the beam must be measured at two points along its path; this allows for precise calculation of its size, shape, and direction of travel.

In the past, experimenters scanned a detector back and forth across the beam in the vertical and horizontal directions in one millimeter increments at two different positions in order to gather data on the beam shape and axis direction. The whole process took about four hours, which amounts to a significant drain on precious beam time and opens the door to a number of systematic errors.

During the spring semester of 2017, Tianqing Zhang, a Duke undergraduate, worked on developing a new detector and electronics system for measurements of the cross-sectional profile and beam axis direction [Zha17]. The detectors he used were neatly packaged in 2-in. by 3-in. arrangements of position-sensitive photomultiplier tubes (PMTs) paired with a specifically matched pre-amplifying circuit. Donated to TUNL by Duke Hospital, the PMTs were coupled to 6-in. by 6-in. arrays of BGO crystal scintillators due to BGO's utility as a PET imaging detector. Although Zhang showed that the system had promise, the BGO scintillators were a significant drawback, because BGO is highly sensitive to γ rays, and the goal of the measurements is to look only at neutrons.

To further refine the concept of using a detector to directly image the neutron beam, we decided to investigate the feasibility of employing plastic scintillating fibers instead of the BGO crystals. TUNL has a long spool of plastic scintillating fiber, so we cut hundreds of 1-in. long segments to couple to a PMT. In order to hold everything together, we designed a piece that is capable of holding a large bundle of fibers directly against the photomultiplier tube using Autodesk Inventor software and 3D-printed it at the Duke CoLab. After a number of tests, we came to the conclusion that the fibers we were using were not a good match for the PMTs. The fibers emit green light, which may have been too low in energy for our PMTs to have a good response. The PMTs respond best to 400 nm light. We also suspect that the fibers, at only 1 mm diameter, were simply too small for their light to spread to more than one of the photocathodes in our PMT, which is of vital significance for position measurements and energy resolution.

Abandoning the scintillating fibers, we decided to go back to using the 2-in. by 3-in. arrangement of PMTs with BGO scintillators. We determined that we could use timing signals to discriminate between neutron and γ-ray events, and this proved to be a valuable step forward. From Fig. 1.7, it is clear that we are able to determine which events were caused

by neutrons based on when our detector fired, and we can make conditional histograms that show us only events that occur within that window.

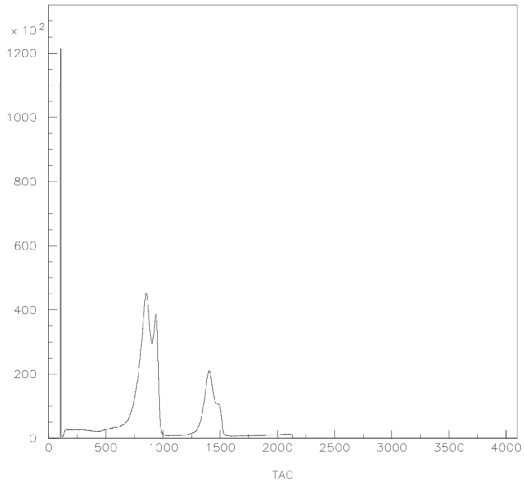

Figure 1.7: Timing spectrum from one run. Two distinct event types can be ascertained based on position in this spectrum. Neutrons form the left peak at around channel 800 and γ rays form the right peak at around channel 1400.

Once we discriminated between neutrons and γ rays and filled histograms with only events related to neutrons, we were able to get excellent results. Figure 1.8 shows the quality of reconstruction we can get after efficiency matching with flat field images, and Figure 1.9 shows how well we can see the beam with respect to its surroundings. Images like these give us the capability of quickly determining a neutron beam's cross-sectional profile and beam axis direction, thus allowing future experimenters to quickly characterize the neutron beam and optimize their experimental setup to match the beam they receive.

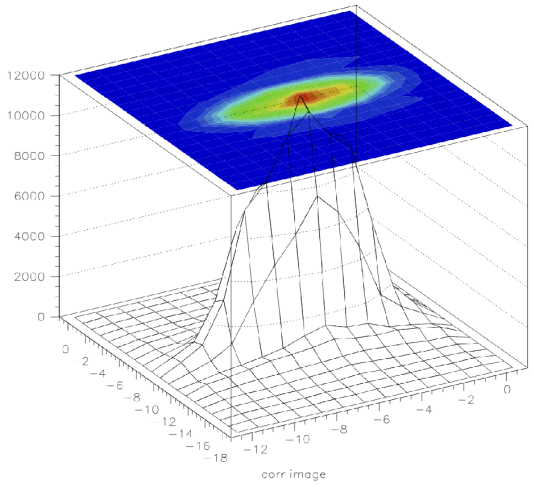

Figure 1.8: Position reconstruction of the neutron beam. The circular beam can be seen near the center of the image.

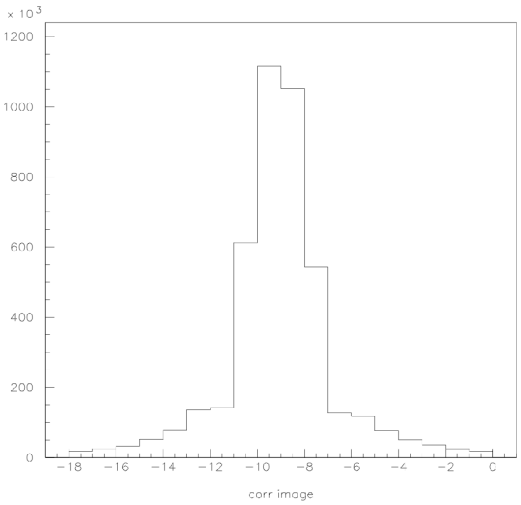

Figure 1.9: Y projection of the X vs Y reconstruction, where Y position is on the X axis. The projection illustrates a large increase in counts within the beam compared to much lower counts on either side.

[Zha17] T. Zhang, C. Howell, and F. Friesen, Independent study final report, Duke University, 2017.

1.4 Determination of Radioactivity in Environmental Samples with $\gamma\gamma$ Coincidence Spectrometry

A. Tillett, *University of North Carolina, Chapel Hill, NC*; J.R. Dermigny, C. Iliadis, *TUNL*

When radioisotopes undergo spontaneous decay, they can release γ rays which can cause harm to living things by interacting with and damaging DNA within cells. The concentrations of several environmental samples, such as Brazil nuts, potting soil, and glossy magazine paper were investigated by use of a $\gamma\gamma$ coincidence spectrometer. The γ-ray emissions of ^{214}Bi and ^{208}Tl were investigated to determine their concentrations and the concentrations of other radioisotopes in secular equilibrium. A Geant4 simulation was used to determine the activities in each environmental sample.

The $\gamma\gamma$ coincidence spectrometer at the University of North Carolina was built to determine radioactive concentrations in different environmental samples. During the decay of ^{238}U and ^{232}Th and their progeny, γ rays can be emitted. In some cases, such as ^{214}Bi and ^{208}Tl, the γ rays which are emitted can be in coincidence with each other, as an atomic nucleus cascades through several excited states within a short period of time as it decays. Through the detection of coincidence events, background radiation is significantly reduced, as most background radiation does not give rise to coincidences.

Three environmental samples, Brazil nuts, potting soil, and glossy magazine paper, were collected and stored in Al sample holders for approximately one month, to ensure the shorter lived progeny were in secular equilibrium with the last long lived radioisotope, ^{226}Ra for the ^{238}U family and ^{228}Th for the ^{232}Th family. Two control samples, BL-4a uranium ore and CRM 107-A monazite sand, were stored in the same way and were used for their well-known activities.

The samples were measured in the spectrometer in twenty-four hour segments for a total time of approximately three days. To determine the important coincidences in the spectrum, the energy deposited in detector 2 versus the energy in detector 1 was plotted. Then, gates on the major coincidence events could be placed (see Fig. 1.10). To determine ^{208}Tl concentrations, energy gates were placed around the 2614 keV characteristic photon, and to determine the ^{214}Bi concentrations, energy gates were placed around the 609 keV characteristic photon.The events that fell in these gates were then projected onto the opposite axes, and 1D histograms could be produced. These histograms were then summed to produce a single 1D histogram of all counts coincident with a certain γ-ray transition.

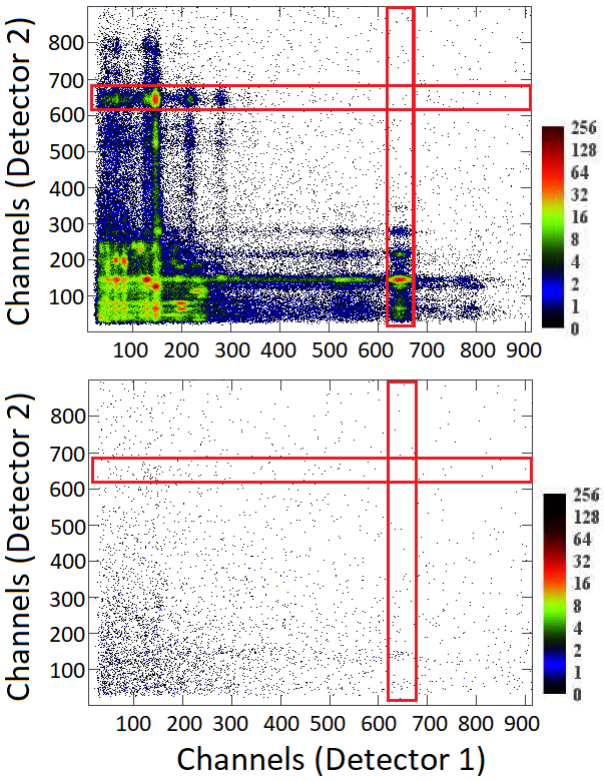

Figure 1.10: The energy gates placed on the coincidences of the 2614 keV photon with other γ rays are shown as red rectangles. The top spectrum corresponds to the monazite sand, and the bottom spectrum corresponds to the Brazil nuts.

Using the summed histogram, the major coincidences can be easily identified. After a running time normalized background is subtracted from the spectra, the net peak counts can be measured in the coincidence peaks. These net counts are the result of radioactive decay within the samples. Using the simulated efficiencies of the spectrometer for each of the samples, activities can be derived for the two radioisotopes. Because of the assumption of secular equilibrium within the sample, the concentrations of ^{226}Ra and ^{228}Th can be inferred. An example of 511 keV and 583 keV photons gated on the coincident transition of 2614 keV in the three environmental samples can be seen in Figure 1.11. The measured activities are listed in Table 1.1.

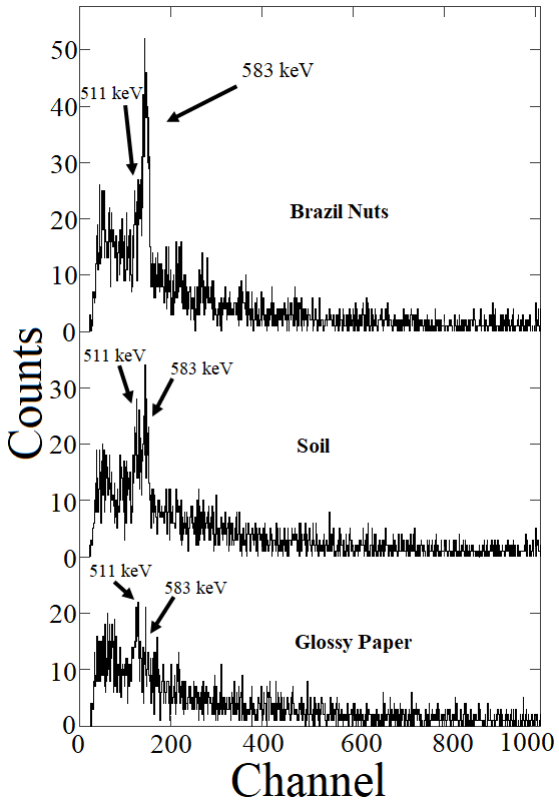

Figure 1.11: The spectra of photons coincident with a 2614 keV photon, showing the 511 keV and 583 keV lines in the three environmental samples.

Monte-Carlo simulations were performed using the GEANT4 toolkit to determine the coincidence efficiencies of the spectrometer for the different samples. The entire spectrometer was simulated using GEANT4, including the detectors, shielding, and samples. An energy dependent Gaussian function was convolved with the simulation's resolution, such that it matched that of the physical spectrometer. The elemental compositions of the control samples were based on provided reference certificates and safety data sheets [Ste82], [New14]. The elemental compositions of the three environmental samples were based on USDA standards for the Brazil nuts [US 84], certified reference material averages for soil [Rei12], and the composition of cellulose, the major component of all paper for the glossy magazine paper [Jac97]. For these simulations, we used the decays of ^{214}Bi and ^{212}Bi to approximate the decay schemes of the two isotopes in question. By doing this, branching ratios could effectively be accounted for. With twenty-four million event runs, the efficiencies of the spectrometer for the two control samples were determined to be within 5% of the efficiencies determined by the known activity of the controls.

Table 1.1: The derived activities for ^{228}Th and ^{226}Ra in the three environmental and control samples. The monazite and uranium ore had their activities derived from their weight percent in the sample and their half-lives. The uncertainties in the measurement are derived from counting statistics only.

Sample	Element	Activity (mBq/g)
Monazite	^{228}Th	4200 ± 200
Brazil Nuts	^{228}Th	21 ± 1
Soil	^{228}Th	10 ± 1
Glossy Paper	^{228}Th	1.3 ± 0.2
Uranium Ore	^{226}Ra	15400 ± 600
Brazil Nuts	^{226}Ra	35 ± 2
Soil	^{226}Ra	15 ± 1
Glossy Paper	^{226}Ra	2.4 ± 0.3

[Jac97] M. Jackson, J. Agricult. Food Chem., **45:6**, 2354 (1997).

[New14] New Brunswick Laboratory, *Safety Data Sheet Monazite Sand Ore Materials*, 2014.

[Rei12] C. Reimann and P. de Caritat, Sci. Total Environ., **416**, 239 (2012).

[Ste82] H. Steger *et al.*, *BL-2a and BL-4a: Certified Uranium Reference Ores*, CANMET, 1982.

[US 84] US Department of Agriculture (USDA), *Composition of Foods: Nut and Seed Products: Raw, Processed, Prepared.*, 1984.

1.5 Nuclear Data Evaluation At TUNL

M.S. Narijauskas, *Central Connecticut State University, New Britain, Connecticut*; J.H. Kelley, C.G. Sheu, *TUNL*

As a part of the international Nuclear Structure and Decay Data Evaluators Network, the Nuclear Data Evaluation group at the Triangle Universities Nuclear Laboratory (TUNL) is responsible for evaluations of the nuclides in the mass range A=3–20. An evaluated nuclear structure and decay data file for ^{20}C and ^{10}N were compiled and submitted to the National Nuclear Data Center(NNDC). Experimental Unevaluated Nuclear Data List files were compiled and submitted to the NNDC from journal articles on ^{10}N [Hoo17] and ^{10}Be [Joh17].

The dissemination of experimental and theoretical information gathered in nuclear research is of critical interest in the nuclear science community. Such data must be evaluated and reviewed for future reference. The nuclear data evaluation group at TUNL assembles nuclear structure data corresponding to nuclides of the atomic mass range A=3–20. Activities include surveying peer-reviewed journal articles, compiling nuclear structure and decay data results into the experimental unevaluated nuclear data list (XUNDL), and creating evaluated nuclear structure data files (ENSDF) for National Nuclear Data Center (NNDC) databases. The exotic nuclides ^{20}C and ^{10}N were surveyed and an ENSDF was submitted. TUNL is also responsible for updating XUNDL files for nuclides in the range mentioned above. A XUNDL file was submitted from journal articles [Hoo17] and [Joh17] corresponding to ^{10}N and ^{10}Be respectively.

Evaluated Nuclear Structure Data File

The ENDSF database files contain information pertaining to nuclear structure and decay data in a standard format provided by the NNDC. Many nuclear experimental journal articles, which can be referenced from the NNDC, are compiled into a structured file in accordance to the Evaluated Nuclear Structure Format Manual located on the NNDC. These files also contain links to theoretically-based journal articles pertinent to the nuclide being discussed. This task was completed for the the nuclides ^{20}C and ^{10}N.

Tables of adopted (recommended) level energies and properties for levels that have been observed in various nuclear reactions and decays can be accessed in the ENDSF files. The half lives of 26.3 ms and 6.8 ps were included in ^{20}C for the ground state and 2+ excited state respectively. The evaluated file for ^{10}N contained adopted levels for the resonances pertaining to the ground, 1-, and 2- states with energies of 3.1, 2.3, and 2.0 MeV respectively. Adopted values were provided and referenced for the TUNL Nuclear Evaluation Database. These values were calculated from a weighted average of values from numerous journal articles. Level schemes present in the ENSDF file display these values in a visual representation. An example can be seen in Figure 1.12.

Information within the NNDC database pertaining to evaluated files is updated regularly by an expert team of evaluators in correspondence with data centers responsible for certain mass ranges.

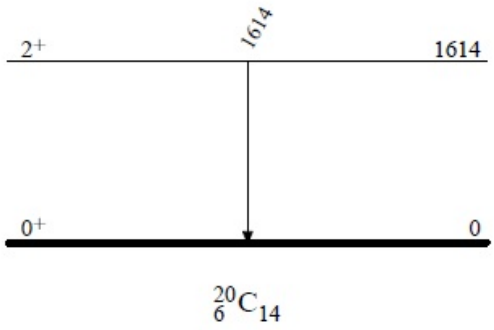

Figure 1.12: Energy values for ^{20}C in the reaction ^{1}H(^{20}C,^{20}Cγ) are plotted vertically in keV, based on the ground state as zero.

When compiling an ENSDF, previously written XUNDL files must be included and incorporated. Each XUNDL is reviewed and edited before inclusion.

^{20}C had four such XUNDL references which were incorporated (see Table 1.2). Some exotic nuclides may not have XUNDL reports written on them. This was the case for ^{10}N.

Table 1.2: XUNDLs used for ^{20}C ENSDF

Dataset	Last Revised	Article
C(^{36}S,Xγ)	2008-10	[Sta08]
^{1}H(^{20}C,^{20}Cγ)	2009-02	[Ele09]
^{9}Be(^{22}O, ^{20}Cγ)	2011-10	[Pet11]
Ta(^{48}Ca,^{20}C)	2012-12	[Gau12]

Experimental Unevaluated Nuclear Data List

The XUNDL dataset is generated from a individual journal article or articles that are from the same experimental group pertaining to similar information. Researchers can also submit material in support of their papers which is incorporated into the XUNDL dataset. Data compilers and authors work together to accomplish this goal. The XUNDL database is updated regularly as new published journal articles are released. Two recent journal articles on ^{10}N [Hoo17] and ^{10}Be [Joh17] were compiled and submitted to the NNDC.

[Ele09] Z. Elekes *et al.*, Phys. Rev. C, **79**, 011302 (2009).

[Gau12] L. Gaudefroy *et al.*, Phys. Rev. Lett., **109**, 202503 (2012).

[Hoo17] J. Hooker *et al.*, Phys. Lett. B, **769**, 62 (2017).

[Joh17] J. G. Johansen *et al.*, J. Phys. G, **44**, 044009 (2017).

[Pet11] M. Petri *et al.*, Phys. Rev. Lett., **107**, 102501 (2011).

[Sta08] M. Stanoiu *et al.*, Phys. Rev. C, **78**, 034315 (2008).

1.6 Noble Gas Leak Detector for Use in the Neutron Electric Dipole Moment Experiment

C.R. Barrow, *North Carolina State University, Raleigh, NC*; P.R. Huffman, K.K.H. Leung, E. Korobkina, C.R. White, *TUNL*

The experiment to find a permanent electric dipole moment of the neutron (nEDM) will employ a large volume of liquid helium housed by a number of helium-permeable composite materials. It is desirable to construct a leak detector that can employ test gases other than helium. The purpose of this project is to create a leak detector that can quantify the argon gas flux in a high vacuum environment and interpret this flux as a leak-rate. This apparatus will be used to check the nEDM volumes for leaks at room temperature before cooling down to cryogenic temperatures. Through device construction and software programming, we were able to build an argon-based leak detector that could check composite and polyamide vacuum volumes for leaks in the range 10×10^{-9} to 10×10^{-5} mbar·l/s.

Common practice for leak-checking high vacuum systems uses helium as the probing gas. However, helium may permeate some materials at room temperature, making leak characterization difficult. The full-scale experiment to find the permanent electric dipole moment of the neutron (nEDM), to be conducted at Oak Ridge National Laboratory, will employ large volumes of liquid helium, housed in non-metallic materials. These materials (specifically G10 and Kapton) are known to be helium-permeable at room temperature [Col]. This permeability is on the order of unacceptable leak-rates for the system. It is, therefore, necessary to develop a means of leak-checking the systems using a probe gas other than helium. In this project, we designed and built a leak detector which uses argon as the probe gas, and could be used to probe with other gases with atomic masses less than 100 amu.

In order to track changes in the amounts of gas within the target vacuum system, we used a Stanford Research Systems (SRS) Residual Gas Analyzer (RGA). The RGA is a quadrupole mass spectrometer which ionizes gas molecules and steers them to a Faraday cup where they are counted in Amperes as an ion current. The internal SRS RGA software then converts this current into a partial pressure. We use this partial pressure to track changes in the gas flux while introducing argon as a spray or external bath. This change in flux can be converted to a leak-rate by multiplying the change in partial pressure by the pumping factor of the leak detector system. This pumping factor is a function of total system pressure and partial pressure for the gas being tested, and is determined empirically, using calibrated leaks.

The calculations necessary to make the leak-rate conversion are built into the Graphic User Interface (GUI). The GUI was programmed in LabView and uses some of the VI's provided by SRS. A screenshot of the GUI is shown in Fig. 1.13.

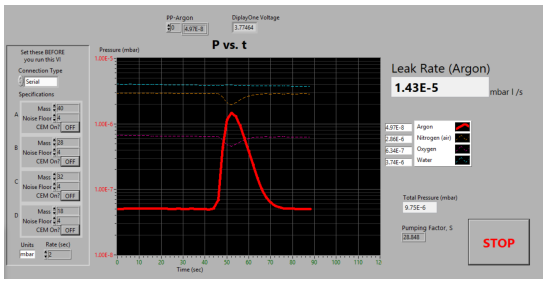

Figure 1.13: A screenshot of the LabView GUI that gives a calculated leak-rate as well as a graphical interpretation of the partial pressure of argon relative to the partial pressures of gases common to air.

The sensitivity of this leak detector is dependent on the background partial pressure of the probe gas present in the target system when leak-checking is conducted. However, the leak detector typically has a background partial pressure of argon of 10^{-10} mbar·l/s, which corresponds to a leak-rate sensitivity of around 3.0×10^{-09} mbar·l/s (argon). Using the conversion

$$Q_{He} = QAr\sqrt{\frac{M_{He}}{M_{Ar}}} \tag{1.2}$$

where Q is a leak rate for the gas in question and M is the mass of the gas, gives our leak detector a minimum sensitivity of around 9×10^{-10} mbar·l/s (helium).

The accuracy of the leak detector is limited to the characterization of the pumping factor of the system. This is presently poorly characterized beyond a factor of 10x, which leads to an accuracy for the leak detector of an order of magnitude. This is generally acceptable for the nEDM test dewar currently being used at NC State University and TUNL. So the leak detector is functional and usable with these limitations. Future work includes understanding and characterizing better this pumping factor to improve system accuracy.

The leak detector may need to be periodically calibrated, and contains a valve on which to attach calibrated leaks. We used two NIST-calibrated leaks which were purchased to our gas specifications. They are certified and labeled. Because they do not contain a volume of gas, but require an external argon input, they should not follow an efficiency decay schedule. Both leaks require a precise input of argon gas at 45 psig.

We tested the leak detector on two leaks that had been profiled using a helium leak detector. Table 1.3 summarizes the results of tests with these leaks.. The expected leak-rates were calculated using Eqn. 1.2. As noted, the measured leak-rates fall nearly a full order of magnitude off of the expected leak-rate.

Figure 1.14: Image of the leak detector system (laptop closed - GUI not visible).

Table 1.3: Performance of noble gas leak detector using argon as the probe gas on leaks previously characterized using a commercial helium leak detector.

Source	Measured LR - He (mbar*l/s)	Expected LR - Ar (mbar*l/s)	Measured LR - Ar (mbar*l/s)	Difference from Expected (mbar*l/s)
Pulstar Dewar (IVC @ 150 K)	3.9E-04	1.2e-04	2.0E-03	+1.8E-03
Calibrated Leak	3.0E-05	9.5E-06	1.9E-06	-7.6E-06

[Col] M. C. Collins and D. G. Haase, unpublished.

1.7 Characterization of a Two Ton NaI Scintillator

A.R. Maier, *Linfield College, McMinnville, OR*; P.S. Barbeau, S.C. Hedges, *TUNL*

The COHERENT collaboration is dedicated to measuring Coherent Elastic Neutrino-Nucleus Scattering (CEνNS), an interaction predicted by the standard model that ultimately serves as a background for dark matter detection. In order to observe the predicted N^2 scaling, COHERENT is deploying two tons of NaI[Tl] scintillator to observe CEνNS recoils of sodium nuclei. Before this detector is deployed, all crystals and PMTs must be characterized to understand the individual properties vital to a precision measurement of CEνNS. For this project, a standard operating procedure (SOP) is being developed to characterize each detector based on seven properties that are relevant to the measurement of CEνNS. Preliminary work on the SOP has provided insight for optimizating the methods needed to characterize the ton scale detector given the unusually large volume of scintillator to be deployed for the collaboration.

The COHERENT collaboration has utilized the well-timed neutrino flux at the Spallation Neutron Source (SNS) at Oak Ridge National Laboratory in efforts to observe Coherent Elastic Neutrino-Nucleus Scattering (CEνNS). Given the recent publication of the collaboration's ground-breaking observation of CEνNS in CsI[Na] [Aki17], the next step for the collaboration is to understand the behavior of this interaction. Specifically, the collaboration looks to test the predicted N^2 scaling law: as the nucleus size N increases, the likelihood of a CEvNS interaction increases by a factor of N^2. The collaboration hopes to observe this scaling behavior in liquid argon, germanium, and NaI. Recently the U.S. Department of Homeland Security has given COHERENT nine tons of NaI scintillating crystals to test this prediction. However, before these crystals can be deployed they must first be characterized. Parameters pertinent to COHERENT's measurement include energy scale, energy resolution, low-energy light yield non-linearity, decay time energy dependence, position variance, time variance, and background levels.

Given the importance of discriminating between low-energy nuclear recoils and electron recoils to effectively observe CEvNS in NaI, much effort has focused on low-energy data. In particular, we are studying the nonlinearity of low-energy light yields, decay times, and energy resolution. We expect nonlinearity at lower energies because NaI has a decreasing quenching factor with decreasing energy and thus the light yield will be more efficient at lower energy. In Fig. 1.15 the ratio of the peak-high-value of events to their integral is nearly entirely linear except at low energies. This property is of interest as it implies a slower decay time at lower energies. We see slight nonlinearity in Fig. 1.16 as every spectral peak below 200 keV was biased higher than the expected value given the calibration linear fit. This discrepancy is slight though significant especially as the sub-100 keV energy range is important for discriminating electron versus small nuclear recoils. This property at low energy makes sense as quenching in NaI is decreasing and thus light yield is closer to 100% than at higher energy.

Energy scale is a function of crystal performance and PMT response and thus may vary from crystal to crystal and from PMT to PMT. Therefore, it is imperative for COHERENT to test each crystal-PMT pairing to understand its energy scale properties. Practically, this has been accomplished by matching peaks in event integral histograms with known spectral energy peaks. Figure 1.17 shows the histograms and process used to distinguish peaks as three separate sources with known spectra are placed near the crystal. Though it was useful to use each source individually to distinguish peaks, now that we understand the general shape of this histogram and the energies associated with each peak, it is viable to simply calibrate with a multi-source run. These data also allow us to understand the energy resolution of our crystals as the narrower the peak is in the histogram, the more precise the PMT/crystal pairing is at deciphering energies.

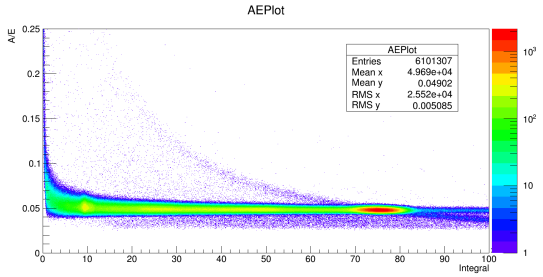

Figure 1.15: Ratio of peak height to integral plotted versus integral for a number of events detected in NaI.

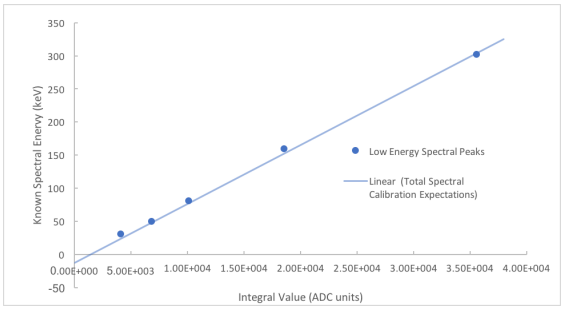

Figure 1.16: Known peak energy plotted vs. the integral of the event.

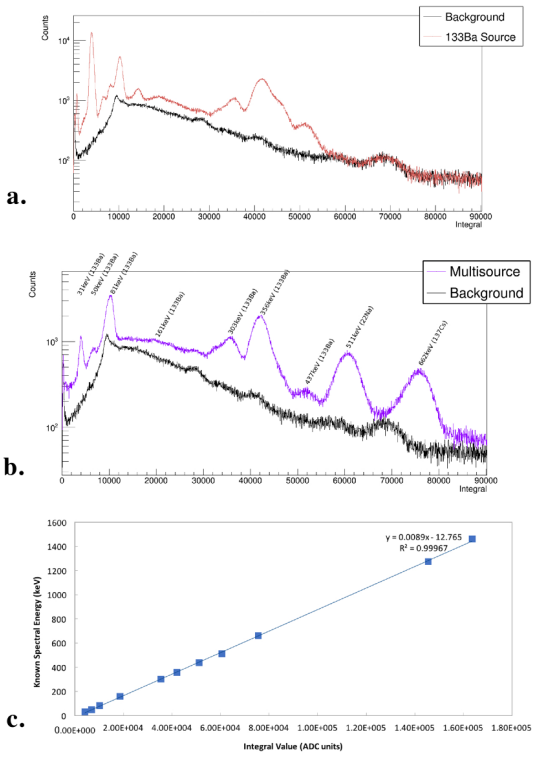

Figure 1.17: (a) Plots of background and ^{133}Ba source spectra. (b) Multi-source run shown with background. (c) Linear fit of peak energy vs. integral of the event.

Finally, we tested each crystal for positional light-yield dependence. We expect small discrepancies in histograms as we collimate sources close to the PMT versus far away because of the slight losses in energy expected of scintillator systems, though if there were to be an incredibly striking drop in light yield from one centimeter to the next, this may indicate a crack in the crystal. In analyzing the plot of peak height divided by energy for sources collimated at 2, 8 and 14 inches from the PMT we find only mild variation in the peaks (see Fig. 1.18). We thus do not expect any cracks or major flaws in this crystal.

We still need to create a SOP for testing time variance and background levels which we expect to be able to analyze with a single, shielded, overnight run. After this is complete, we will be able to fully characterize every crystal and eventually deploy this detector with great precision.

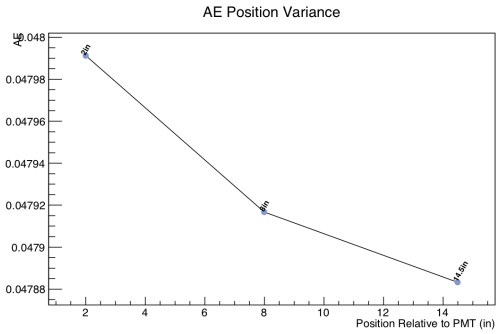

Figure 1.18: Ratio of peak height and energy versus the position of the source relative to the crystal.

[Aki17] D. Akimov *et al.*, Science, **LIII**, 1123 (2017).

1.8 Frequency Domain Multiplexing for NaI[Tl] Detectors

S.W. Belling, *University of Wisconsin - Platteville, Platteville, WI*; P.S. Barbeau, S.C. Hedges, *TUNL*

A process used in many forms of signal communication known as multiplexing is adapted for the purpose of combining signals from NaI[Tl] detectors so that fewer digitizer channels can be used to process the signal information from large experiments within the COHERENT collaboration [Aki17]. Each signal is passed through a ringing circuit to modulate it with a characteristic frequency. Information about the signal can be extracted from the amplitude, frequency, and phase of the signal using a Fourier transform. Our results show that the energy, channel, and time of the original interaction can be recovered by this process. The effort is ongoing, but with the design presented it is possible to multiplex 10 detectors into a single digitizer channel.

The basic premise of multiplexing is to take several signals and combine them into fewer signals while retaining all pertinent information about the original signals. One implementation of this idea is frequency domain multiplexing, where signals are modulated with a carrier wave to give them a characteristic frequency, such as in FM radio. These signals can then be summed together to give one output. By analyzing the frequency content of the output, the energy, time, and channel of original signal can be recovered. In some cases, further signal processing, such as filtering and deconvolution can reconstruct more information from the original signal, but in general there are trade-offs between different methods. In this work, the signals come from NaI[Tl] detectors.

The NaI[Tl] detector is a scintillating crystal attached to a photomultiplier tube (PMT) and a base. Photons are emitted when particles interact with the crystal, and these are detected by the PMT. The PMT converts the photon energy into an electrical signal that then is modified by the base, usually amplified. The electrical signal can then be passed directly into a digitizer where it is converted to a digital signal that can be stored in a binary format. The application of these detectors to neutrino interactions was explored by Suh [Suh16]. On a small scale this is fine; however, in order to implement enough detectors for a large scale NaI detector deployment, the digitizers alone would cost hundreds of thousands to millions of dollars. Multiplexing the outputs from several detectors together would reduce the number of digitizers required, thus reducing the cost dramatically. A similar system is being investigated in Ref. [Mis] for use with organic scintillators.

In order to implement frequency domain multiplexing, the signals from the PMT have to be modulated with carrier waves of a frequency unique to the detector channel, so that the event can be linked to the correct detector. The modulation of the signal is accomplished with an operational amplifier used in the non-inverting configuration with an RLC circuit in the feedback loop as seen in Fig. 1.19. In this figure only one channel is shown, but multiple channels are connected in the same way. The resistor, capacitor, and inductor values will determine the frequency at which the output oscillates. The resistor contributes mainly to the decay of the transfer function of the circuit, so that individual events occur only in a few microsecond time window.

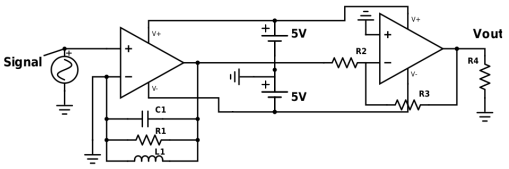

Figure 1.19: The L, R, and C values uniquely determine the frequency at which the output oscillates. The second (right) op-amp sums the signals together.

The ringing output of the multiplexing circuit is what is analyzed in order to recover the original signal information. An example output is shown in Fig. 1.20. A fast Fourier transform (FFT) is used to identify the channel. The amplitude of the decaying sinusoidal function corresponds to the energy of the original signal. The phase from the FFT gives timing information. Each channel was given a different ringing frequency by changing the capacitor

value in the circuit above. For a parallel LRC circuit, the oscillation frequency, ω_t, is given by the following equations.

$$\omega_{LC} = \frac{1}{\sqrt{LC}} \quad (1.3)$$

$$Q = R\sqrt{\frac{C}{L}} \quad (1.4)$$

$$\omega_t = \omega_{LC}\sqrt{1-\frac{1}{4Q^2}} \quad (1.5)$$

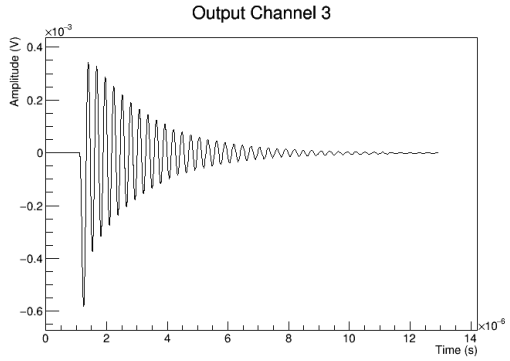

Figure 1.20: The ringing output of the circuit.

From the information shown in Fig. 1.21 and the phase information, the energy, time, and detector for the event can be determined. To test the idea, simulations in LTSpice were performed and the results were analyzed using Python. A breadboard prototype was constructed and tested.

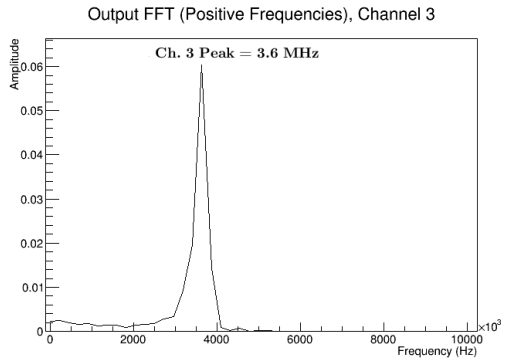

Figure 1.21: Power Spectrum for the ringing output in Fig. 2. The frequency peak corresponds to the expected frequency, calculated from the LRC values.

In some cases it is possible to directly recover the input signal through deconvolution. The transfer function of the circuit is found by applying a square wave input to the circuit and taking the Fourier transform of the square wave and the resulting output. The quotient of the output and input FFTs should give the circuit's transfer function. Then, for a given output, the quotient of the output and the transfer function should give the Fourier domain version of the input. Finally, an inverse FFT can recover the signal. This is represented mathematically in the following equation, where $Y(\omega)$ is the circuit output, $X(\omega)$ is the input, x(t) is the time domain input, and $H(\omega)$ is the transfer function.

$$x(t) = \frac{1}{2\pi}\int_{-\infty}^{\infty}\frac{Y(\omega)}{H(\omega)}e^{i\omega t}d\omega \quad (1.6)$$

However this is more difficult when the output of the NaI Detector has a shorter decay time, because the input to the multiplexing circuit is then close to an impulse. In such a case, a calibration is performed where the energy of the initial signal is compared with the amplitude of the ringing output. Such a calibration is shown in Fig. 4.

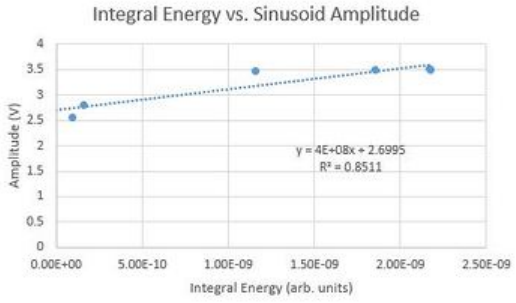

Figure 1.22: Relationship between signal energy and sinusoid amplitude.

While the effort is ongoing, at this point it is possible to multiplex 10 NaI[Tl] signals into one digitizer channel.

[Aki17] D. Akimov *et al.*, Science, page 10.1126/science.aao0990 (2017).

[Mis] M. Mishra, Frequency Domain Multiplexing of Multiple Organic Scintillator Detectors, unpublished.

[Suh16] B. Suh, Senior thesis, Duke University, 2016.

1.9 Development of Data Quality and Analysis Tools for the MAJORANA DEMONSTRATOR

J.H. PARKES, *University of Alabama, Tuscaloosa, AL*; A.L. REINNE, J.F. WILKERSON, *TUNL*

The MAJORANA DEMONSTRATOR is a high-purity germanium (HPGe) detector array consisting of p-type point contact detectors operating 4850 ft below ground in the Sanford Underground Research Facility in South Dakota. The DEMONSTRATOR is designed to search for neutrinoless double-beta decay ($0\nu\beta\beta$) while determining the feasibility of the construction of a future tonne-scale modular detector. The purpose of this work was two-fold: (1) to develop data analysis tools for data validation and time coincidences, and (2) to make a search for α-decay background related coincidences. Our initial search for these coincidences did not find any candidates, indicating very low α-related backgrounds.

It has been theoretically proposed that neutrinos are Majorana particles. While there are many ramifications of this theory, one significant prediction is that the neutrino is its own anti-particle. This would enable the violation of lepton number conservation and thus require an alteration of the Standard Model of Particle Physics. Hence, determining the true nature of neutrinos is of key importance in modern physics. One of the most promising methods of testing this hypothesis is to observe a neutrinoless double beta decay ($0\nu\beta\beta$) within ^{76}Ge. The fact that ^{76}Ge undergoes double beta decay has been well verified. Normally, this process emits two electrons and two anti-electron neutrinos. However, if the neutrino is a Majorana particle, then there is a chance of it only emitting electrons with the virtual particle annihilation of the neutrinos. If this second decay route occurs, then it is significantly less likely to occur than the normal decay route. Based on current experimental results, it is believed that the $0\nu\beta\beta$ decay of ^{76}Ge would be required to have a half-life greater than 10^{25} yrs. As a result, it is necessary for a detector hoping to measure a $0\nu\beta\beta$ decay to maximize its run time while minimizing its background. The MAJORANA DEMONSTRATOR (MJD) is an array of high purity germanium (HPGe) detectors designed to test experimental technologies and analysis methods developed to minimize the background count rate in the energy region of a possible $0\nu\beta\beta$ decay signal [Abg14].

Bias Voltage Analysis

In order to ensure data being collected by the MJD only contains data due to particle decay or interaction within the detector, each of the HPGe detectors is constantly monitored for instabilities. If observed, the HPGe detector is biased down in order to prevent data contamination. Currently, the duration of this biased down state is approximated by the detector operator. However, maximizing run time is critical to increasing the likelihood of detecting $0\nu\beta\beta$ decay. Thus, this project sought to develop a method of tracking bias voltage changes within the detector. A program was created which analyzes the bias voltage of each detector in the DEMONSTRATOR using preprocessed data. If the program detects a change in the bias voltage, it flags the run. An example of the bias voltage across an unstable detector can be seen in Fig. 1.23. A comparison between flagged runs and runs known to contain voltage changes revealed all of the known runs to be flagged, thus indicating the success of the program.

Coincidence Analysis

It has been observed that ^{238}U and ^{232}Th are naturally present in most metals on Earth. These isotopes possess long decay chains of particles with a range of half-lives and energies which undergo γ, α, or β decay. Fortunately, events in MAJORANA caused by α decay can be removed from data sets via precision waveform discrimination. However, because MAJORANA is searching for β signals, this method cannot be used to eliminate the daughter particles of ^{238}U and ^{232}Th which undergo β decay.

That being said, within both the ^{238}U and ^{232}Th decay chains there are known coincident α-β and β-α decays. Thus, it may be possible to locate β decays associated with radioactive contaminants by search-

ing for events which are coincident with an α particle. Recent results by a student at UNC at Chapel Hill suggested that a multitude of events detected by the DEMONSTRATOR were coincident with α events [Nan17].

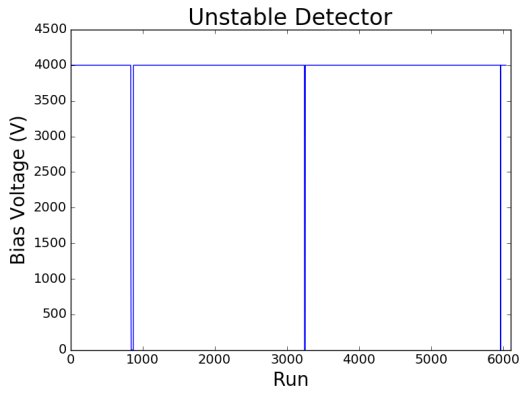

Figure 1.23: Depicted is the bias voltage accross an individual unstable HPGe detector. Despite being biased down a few times, for the majority of the runs the detector appears to maintain a constant bias voltage.

This project sought to create a coincidence analysis method capable of eliminating β decays due to radioactive contaminants. This was achieved by developing a PyROOT program which analyzes timing and energy conditions of events within the MAJORANA data. Upon running, the code detected no apparent coincidence events within the time interval 300 ns to 2 s. This observation deviates from the previous results. Further investigation revealed that the discrepancy was due to updated data cleaning procedures designed to remove events believed to result from detector instabilities. An example of an instability called a noisy burst is depicted in Fig. 1.24. Noisy bursts are believed to be the result of phenomena unrelated to the physics of $0\nu\beta\beta$ decay. The run in Fig. 1.24 appears to be the result of high voltage breakdown within one of the detectors.

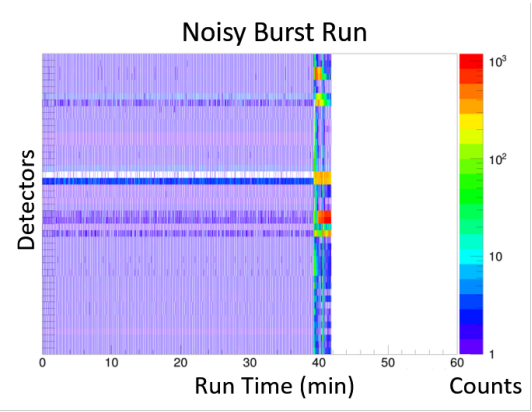

Figure 1.24: Depicted is a noisy burst which is believed to be a result of high voltage breakdown. If not eliminated from the data sets, random coincidences can occur from non-physics events seen here at 40 minutes.

Conclusions

The discovery of $0\nu\beta\beta$ decay would revolutionize physics. This project sought to help in this endeavor through the development of data quality and analysis tools for the MAJORANA DEMONSTRATOR. First, a program capable of flagging changes in the bias voltage of any of the HPGe detectors was created. When implemented, this code will enable the MAJORANA Collaboration to increase the live time of the detectors. Beyond this, the project attempted to develop a code capable of locating coincidence events due to radioactive decay. This investigation suggests that less radioactive isotopes are present within the MAJORANA DEMONSTRATOR than supposed by previous studies.

[Abg14] N. Abgrall *et al.*, Adv. High Ener. Phys., **2014**, 1 (2014).

[Nan17] J. Nance, Senior honors thesis, Univesity of North Carolina at Chapel Hill, 2017.

1.10 Modeling Neutral-Current Neutrino Interactions in Liquid Argon

C. Nunez, *Florida International University, Miami, FL*; K. Scholberg, E. Conley, *Duke University, Durham, NC*

Studies of supernova neutrinos provide knowledge of supernova physics. The Deep Underground Neutrino Experiment (DUNE) will use a Liquid Argon Time-Projection Chamber (LArTPC) which will be able to detect charged-current, neutral-current, and elastic-scattering interactions to study the dynamics of supernova. The neutral current ν-^{40}Ar interaction leaves an excited ^{40}Ar nucleus that releases a 9.8 MeV γ ray. This project creates a smearing file for SNOwGLoBES, an event rate calculator, that corresponds to the DUNE detector simulation for a 9.8 MeV γ ray. The expected number of neutral current supernova neutrino events in liquid ^{40}Ar is determined and the observable energy distribution is examined.

A supernova burst creates large amounts of neutrinos that will be studied with the Liquid Argon Time Projection Chamber (LArTPC) at the Deep Underground Neutrino Experiment (DUNE). The LArTPC will be able to detect charged-current(CC), neutral-current(NC), and elastic scattering(ES) interactions [Sch12]. The NC ν-^{40}Ar interaction is analyzed for the DUNE detector simulation. This interaction leaves an excited ^{40}Ar nucleus that releases a 9.8 MeV γ ray as it returns to the ground state.

SNOwGLoBES is used to analyze the event rate and observable energy distributions for the interaction. SNOwGLoBES reads in the supernova flux, cross sections, detector smearing, and post-smearing efficiencies to output the smeared rates (events as a function of detected energy) [Bec14].

The NC cross section file used for SNOwGLoBES is calculated by Dr. Anna Hayes [Hay17] ranging from 5 MeV to 100 MeV. Since NC ν-^{40}Ar does not depend on the flavor of the incoming neutrino, the cross section is set the same for all the different flavors.

The smearing file is developed from a simulation of detecting the 9.8 MeV γ ray in the LArTPC. Erin Conley simulated several 9.8 MeV γ rays using LArSoft. The γ rays are isotropic and uniform and no noise is added. The charge is added up and a distribution is made. Using the charge-energy relationship found by Erin Conley, the distribution of energy deposition is acquired (see Fig. 1.25). The energy distribution is interpolated to get the correct number of bins (200 bins, with energy range 0 to 100), smoothed, and normalized for the smearing file. Each column of the smearing matrix is filled with the normalized energy distribution since a 9.8 MeV γ ray will be produced for all incident energies of the neutrino.

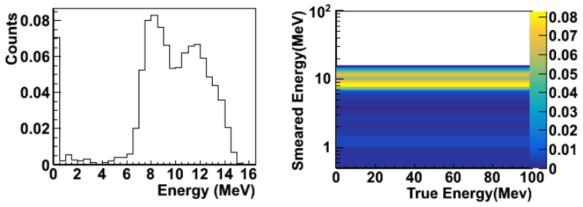

Figure 1.25: Interpolated, smoothed, normalized energy deposition distribution is filled into each column of the smearing matrix. The mean of the energy deposition distribution is 9.3 ± 3.4 MeV.

Assuming 100% post-smearing efficiency above 5 MeV threshold, the GKVM supernova model flux [Gav09] smeared event rate is calculated using SNOwGLoBES (see Fig. 1.26). A plot of the total event rates show that it will be difficult to distinguish the NC events from the CC events. This demonstrates the importance of being able to separate the 9.8 MeV γ rays from the electrons in the detector.

Due to impurities in liquid ^{40}Ar, the electrons will lose energy before reaching the TPC wire plane. Drift correction can be applied in order to know more about the original energy of the electron. Knowing Monte-Carlo truth information, a truth drift correction is done on the 9.8 MeV γ-ray simulation. The energy distribution is acquired with the same charge-energy relationship, and then is interpolated to get the correct number of bins for SNOwGLoBES, smoothed, and normalized for the smearing matrix. The smearing matrix has each column filled with the

normalized energy distribution with drift correction (see Fig. 1.27).

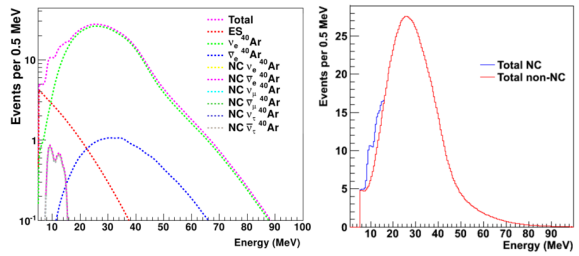

Figure 1.26: The event rates for the GVKM supernova flux model. Various interactions in liquid ^{40}Ar are shown with the on a log scale (left panel). The right panel shows the total events with and without the neutral current.

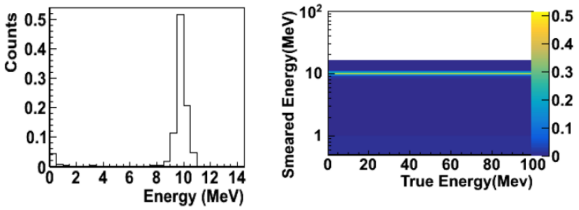

Figure 1.27: Interpolated, smoothed, and normalized truth drift corrected energy deposition distribution is filled into each column of the smearing matrix. The mean of the truth drift corrected energy deposition distribution is 9.2 ± 2.4 MeV.

The event rates are analyzed for the GKVM model and the drift-corrected smearing file. Assuming 100% post-smearing efficiency above 5 MeV threshold, the GKVM flux drift-corrected smeared event rate is calculated using SNOwGLoBES. Results show that there is a large peak for neutral-current events at around 9.8 MeV for the total smeared event rates, which is more noticeable compared to the other interactions. This demonstrates the importance of having drift correction in the detector (see Fig. 1.28).

In addition, the total smeared event rates are calculated for various pinched supernova fluxes. The flux of a supernova is described by the average neutrino energy and the pinching factor (α) [Sch12]. The SNOwGLoBES program reads in neutrino energies, pinching values, and luminosity to create different supernova pinched fluxes. Running SNOwGLoBES with the NC-smeared files and calculating the total smeared event rates demonstrated that there are more NC ν-^{40}Ar for supernova fluxes with higher energies and lower values of α.

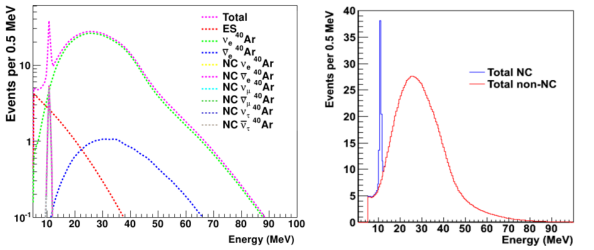

Figure 1.28: The event rates for the GVKM supernova flux model for the detector simulation with drift correction. Various interactions in liquid ^{40}Ar are shown on a log scale (left panel). The right panel shows the total events with and without the neutral current.

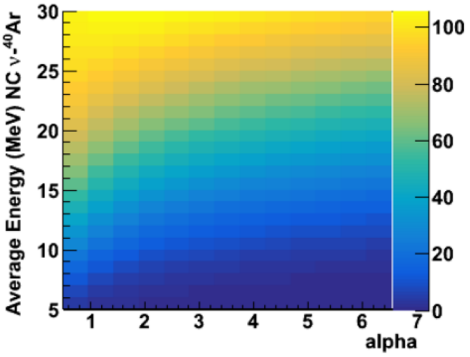

Figure 1.29: Total NC event rates for the different pinched fluxes by ranging the pinching factor from 0.5 to 7 and the neutrino energy from 5 MeV to 30 MeV for all neutrino flavors. The luminosity for all flavors is set to 2.5 × 10^{52} ergs/s.

The simulation in LArSoft shows the importance of being able to separate the 9.8 MeV γ rays from the electrons in the LArTPC and having a drift correction in the detector for future physics studies. Additional work to be done includes adding noise into the simulation, selecting events to find out more about the energy deposition, and applying the drift correction with reconstructed energy information.

[Bec14] A. Beck *et al.*, *SNOwGLoBES: SuperNova Observatoris with GLoBES: Draft*, 2014.

[Gav09] J. Gava *et al.*, Phys. Rev. Lett., **103**, 071101 (2009).

[Hay17] A. Hayes, 2017, private communication.

[Sch12] K. Scholberg, Ann. Rev. Nucl. Part. Sci., **62**, 81 (2012).

Research Based at CERN

Chapter 2

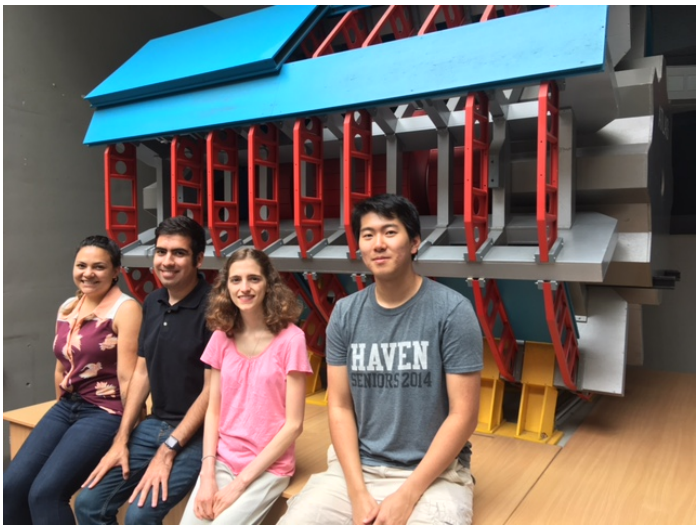

2.1 The Search for New Particles Decaying to W+γ Final States

T.M. Contreras, *University of Oregon, Eugene, OR*; A.T. Goshaw, *Duke University*

The ATLAS experiment searches for evidence of new particles by using proton-proton collisions in the Large Hadron Collider. Our search focuses on a possible particle X, that may explain phenomena not described by the Standard Model (SM). We look at the decay of particle X to a W boson and a photon. We simulate SM interactions in the ATLAS detector via Monte-Carlo techniques, then compare our analysis on Monte-Carlo simulations and our analysis of data from the ATLAS detector. Any significant differences between predictions and data will provide evidence for a particle not described by the SM. Our results show that the transverse momentum distributions for simulated and real data particles match fairly well, as does the reconstructed mass of the W boson.

Physics Beyond the Standard Model (BSM) may describe a new force with a new carrier. A proposed carrier for a generic BSM force is the heavy boson X. This boson is postulated to have two main decay channels: $X^{\pm} \to Z^{\pm} + \gamma$ and $X^0 \to W^0 + \gamma$ [Eic08]. This study will focus only on the $X^0 \to W^0 + \gamma$ channel, specifically on the final state where $W \to \mu + \nu$. This study uses data from the ATLAS detector and compares it to a simulation from the Sherpa generator [Gle09] to search for the BSM particle X. The data was taken in the 2016 run, with proton-proton collisions and a center of mass energy of 13 TeV. A trigger for a high-momentum muon was then applied to the data. The simulation is a Sherpa 2.2.2 $W(\mu, \nu) + \gamma$ generator.

The Sherpa simulation has a parton level that uses only the Standard Model theory to generate events from a proton-proton collision, and a reconstructed level that takes those generated events and simulates how they would look in the ATLAS detector after digitization. An extensive comparison of the parton and reconstructed levels of the Sherpa simulation was done to best understand the simulation.

Analysis of both the Sherpa simulation and the data used the standard ATLAS xAOD RootCore packages. For the simulated parton level information, we select one photon, one muon, one neutrino, and either one gluon or one quark based on the maximum transverse momentum for every event. For the simulated reconstructed model and for the data, we select one photon, one muon, based on the maximum transverse momentum, and reconstructed the missing transverse momentum (E_T^{miss}) per event. The E_T^{miss} is the imbalance of energy in the detector for one event, and for this study we are attributing the E_T^{miss} to the neutrino. Using the angle of separation:

$$\Delta R = \sqrt{(\eta_1 - \eta_2)^2 + (\phi_1 - \phi_2)^2} \qquad (2.1)$$

we select the jet with the maximum transverse momentum that also had a $\Delta R(\gamma, jet) > 0.2$, to avoid selecting a photon that was incorrectly identified as a jet. We then created a smaller data file containing just these particles to run over the events more quickly.

Table 2.1: Kinematic cuts are applied to decrease background. Monte-Carlo (MC) simulation matching cuts are applied only when comparing parton and reconstructed levels.

Particle	Kinematics		MC Matching	
	p_T [GeV]	$\lvert\eta\rvert$	ΔR	Δp_T^*
γ	> 15	< 1.37 or (1.52,2.37)	< 0.2	< 0.3
μ	> 25	< 2.4	< 0.2	< 0.3
ν or E_T^{miss}	> 35	< 2.4	-	-
Max(q,g) or jet	> 30	-	-	-

With these smaller files, we made kinematic cuts to increase the efficiency of selecting the particles of interest and to decrease background. When comparing simulated parton and reconstructed information, we also made matching cuts. All cuts are summarized in Table 2.1. We first made comparisons of the parton level to the simulated reconstructed level. The

results in Fig. 2.1 show that the reconstructed distribution matches the parton level information fairly well.

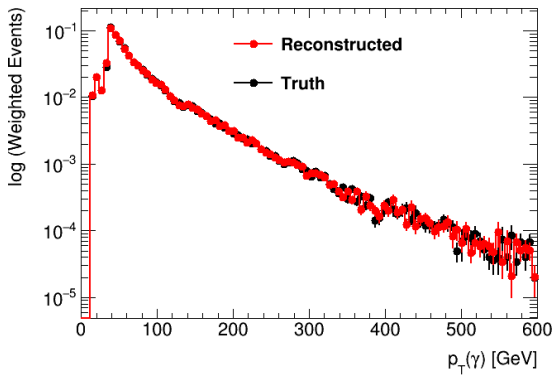

Figure 2.1: Transverse momentum distribution of the truth and reconstructed levels for the Monte-Carlo simulation for the photon.

Next, we compare the simulation to data from the ATLAS detector. First, we compare the transverse momentum distributions from the simulation to real data (see Fig. 2.2).

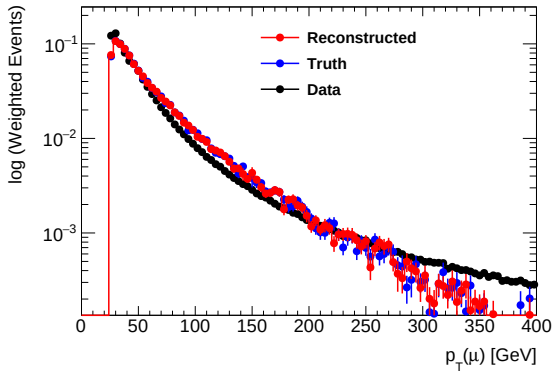

Figure 2.2: Transverse momentum distribution of the muon.

The next step was to reconstruct the mass of the W boson from the muon and neutrino. Since the neutrino is only seen in the detector as missing transverse energy, we can only reconstruct the transverse mass of the W when using the muon and neutrino. It is an appropriate estimation to assume that the muon and neutrino are massless in these calculations, which results in $E_T = p_T$. With massless daughter particles, the transverse mass of the parent W boson is as follows:

$$M_T(\mu,\nu) = E_{T,\mu}E_{T,\nu}(1 - cos(\Delta\phi_{\mu,nu})) \qquad (2.2)$$

where the $\Delta\phi_{\mu,\nu}$ represents the transverse spearation angle between the muon and neutrino. In the simulated reconstructed information and in the data, the neutrino energy would be replaced with E_T^{miss}.

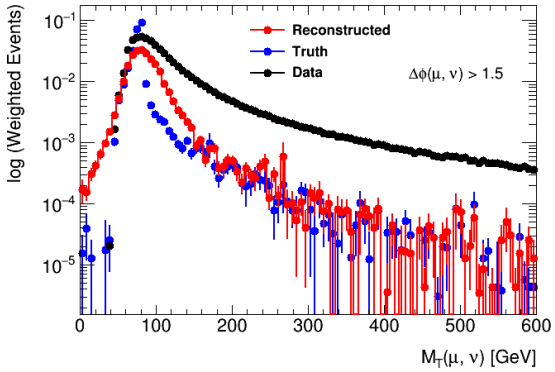

Figure 2.3: Transverse mass of the W boson reconstructed from a muon and neutrino, using Eqn. 2.2.

Figure 2.3 shows that both the simulation and data give peaks at the W mass. An additional cut of $\Delta\phi(\mu,\nu) > 1.5$ was made to both the simulation and data due to large peaks at zero from the events where the muon and neutrino are very close together.

The results of this study show that the simulation truth and reconstructed levels match very well. We also find that the data is consistent with the p_T distributions for the simulation photon, muon, neutrino, and quark/gluon. The comparison of the reconstructed transverse mass of the W boson from the muon and neutrino showed a similarity, but with very different tails that could possibly disappear after proper weighting of the events, as well as getting rid of further background not accounted for in this study.

Future work includes finding the integrated luminosity for the data in order to correctly weight the data to the Monte-Carlo simulation. Then further comparisons of the positions of particles and differences in transverse momentum can be made.

[Eic08] E. Eichten and K. Lane, Phys. Lett. B, **669**, 235 (2008).

[Gle09] T. Gleisberg *et al.*, JHEP, **02**, 007 (2009).

2.2 Study of Charged Particle Distributions in Gluon-Enriched Jet Samples

M. M. Flores, *New Mexico Institute of Mining and Technology, Socorro, NM*; A.T. Arce, *Duke University*

The analysis of distributions of neutral and charged track pairs, in addition to the application of cuts based on rapidity gap, may provide insight into discovering low mass candidates for glueball particles, which have been theorized by Quantum Chromodynamics since its inception. In this project, event, jet, and track selection were all performed on Monte Carlo and detector data. Comparison between analysis with and without the rapidity gap cut was then performed. Differences between Monte Carlo and detector data prevented a direct comparison between the two. However, comparison of detector data with and without the rapidity gap cut does not suggest a model interdependent result.

Historically, the difference between the distributions of neutral and charged track pairs has led to the discovery of new particles. Figure 2.4 shows how example data can be used to identify the ρ meson using this methodology. In our work, this procedure was modified to require a rapidity gap threshold, as suggested by Ochs [Och13] and attempted in experiments by DELPHI [DEL06]. The inclusion of such a cut and the tagging of the initiating particle has enabled the search for particles which may resemble low mass glueballs as theorized by Quantum Chromodynamics.

The study began with the selection of valid tracks. The cut parameters were mirrored from charged particle multiplicity studies performed by the ATLAS collaboration [ATL16]. Further event selection involved the inclusion of the rapidity gap cut. This cut was based heavily on the ee^- experiments performed by the DELPHI collaboration [DEL06]. For any given event, the jet with the largest transverse momentum (p_T) was labeled as the leading jet. Following this, the relative rapidity was then computed for tracks associated with any jet in the event. This was done with the following relation:

$$y_{\text{rel}} = \frac{1}{2} \ln \left(\frac{E + \mathbf{p} \cdot \hat{\mathbf{z}}}{E - \mathbf{p} \cdot \hat{\mathbf{z}}} \right) \tag{2.3}$$

Here, $\mathbf{p}$ represents the 3-momentum of a given track and $\hat{z}$ is a unit vector in the direction of the 3-momentum of the leading jet. Subsequently, the track with the largest relative rapidity was labeled the leading track for its parent jet. The difference in relative rapidity between the leading track and the lower rapidity tracks was taken. If any track pairs had a relative rapidity difference less then one, then the enclosing jet was considered invalid.

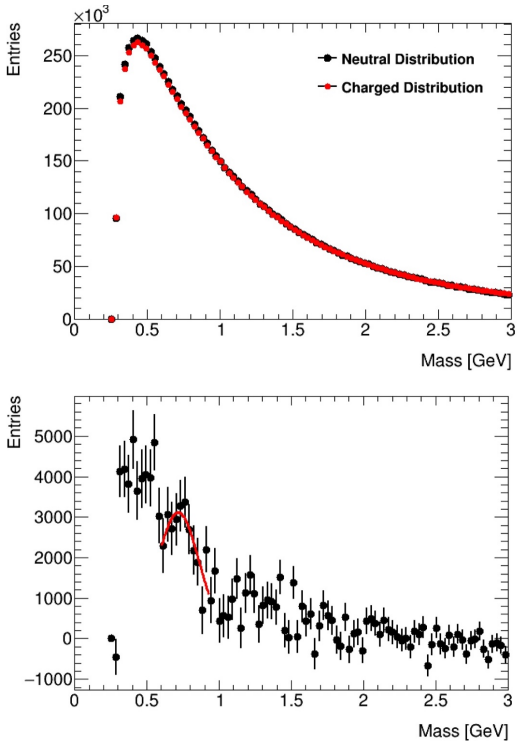

Figure 2.4: Top: Neutral and charged track pairs distribution. Bottom: The difference between the neutral track pairs distribution and charged track pairs distribution. Here, the ρ meson is identified at $\sim$ 775 MeV.

In addition to the applications of cuts, jets were tagged with their respective initiating particle. Both Monte Carlo (MC) and detector data required the implementation of weak quark-gluon cut. Similar to

before, the leading jet was identified for a given event. Similarly, the jet with the second largest transverse momentum was tagged as the sub-leading jet. If the energy of the leading jet was 1.5 times less than that of the sub-leading jet, then the event was discarded. Following this procedure, the jet with the smallest absolute pseudorapidity was tagged to be a gluon jet [Gal11]. This process can only assign quark/gluon tags to the leading and sub-leading jets of a given event. Therefore to match this restriction, the leading and sub-leading jets are only considered when using both the detector data and the MC data.

The analysis discussed was applied to both MC runs and detector data. The MC data was split among numerous other files, each for a predefined transverse momentum range (see Fig. 2.5). Further, the MC generator applied event weights for each separate file. This required accessing and applying MC generator weights upon filling the output histograms of our analysis. An additional weight was applied to each of the MC data files. This per-event weight, is defined as

$$\text{Per-Event Weight} = \frac{L\sigma\varepsilon}{N} \tag{2.4}$$

where L is the luminosity (assumed to be 32000), σ is the cross section, ε is the filter efficiency and N is the number of events processed.

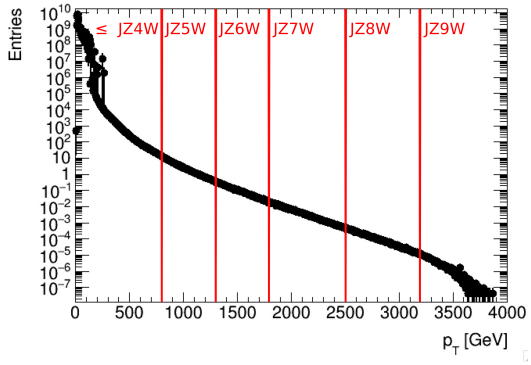

Figure 2.5: Transverse momentum distribution reconstructed into nine individual MC data files. The red lines indicate the p_T ranges for each file.

This final process allowed for the generation of the two four-plot panels shown in Fig. 2.6. The difference between the detector data and MC data presented in Fig. 2.6 are dramatic. Due to time constraints this stark difference could not be investigated. One potential reason of the variance could be the differences in the average jet energy between MC and detector data. This discrepancy, caused by the triggers, could be the source of the unusual distributions seen in the MC data. An additional source of error could be the way the MC simulations identify positive and negative tracks. Regardless of the issue, this prevents a direct comparison between MC and detector data. However, comparing only detector data with and without the rapidity gap shows that the rapidity gap cut produces no visible resonances. This methodology can not fully be disregarded until issues with the discrepancies with the MC and detector data are settled and a more strict quark-gluon tagging is implemented.

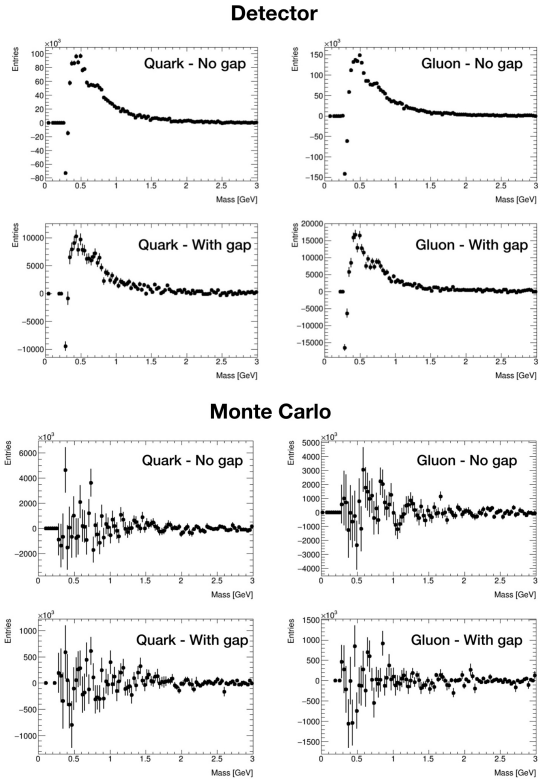

Figure 2.6: Result of the analysis with detector data (top) and MC data (bottom). Major differences between the outputs could be causing such a vast difference between the detector and MC data.

[ATL16] ATLAS Collaboration, Eur. Phys. J. C, **76**, 322 (2016).

[DEL06] DELPHI Collaboration, Phys. Lett. B, **643**, 147 (2006).

[Gal11] J. Gallicchio and M. Schwartz., JHEP, **10**, 103 (2011).

[Och13] W. Ochs, J. Phys. G, **40**, 043001 (2013).

2.3 Data Monitoring of the Transition Radiation Tracker at the ATLAS Experiment

E. Le Boulicaut, *Gustavus Adolphus College, Saint Peter, MN*; M. Kruse, A. Bocci, *Duke University*

The Transition Radiation Tracker provides tracking and particle identification information for the ATLAS detector. Data monitoring during and immediately after a run is essential in order to avoid losses of possible physics results due to detector malfunctions. Our work consists in assisting this data monitoring process by summarizing raw data plots to create a more visual and intuitive representation. This procedure makes locating and identifying potential defects easier and could be applied to a wide range of raw data plots.

The Transition Radiation Tracker (TRT) is a part of the ATLAS detector located in the inner region, closest to the beam. Its primary role is for tracking, but it also provides some particle identification information, which is then validated by other ATLAS sub-detectors. The TRT barrel (region closest to the interaction point) is subdivided into 32 sections in the ϕ direction [a], called stacks. Each stack contains six circuit boards, holding a total of 104 read-out chips. Finally, each chip holds 16 gas tubes, called straws [Han09].

When a particle passes through a straw, it ionizes the gas, thus releasing electrons which then travel to a wire in the center of the straw and produce a signal which exceeds a Low Threshold (LT). When this threshold is crossed, a straw is said to register a "hit". Multiple "hits" in adjacent straws are used for track reconstruction [Kli08].

The goal of this work was to aid in data monitoring by summarizing a large number of raw data plots into a single visual and intuitive picture of the TRT detector, making it easier to locate and identify potential defects.

The process for obtaining such a visual summary was based on a single raw data plot named "Any LL bit: Chips". This essentially describes the occupancy, or the probability of a chip registering a LT hit in a given stack. First, a stack-by-stack comparison with a reference run was undertaken. We started by scaling the test data to match the reference data, thus accounting for different luminosities. Then, for each point in the plot, a t-value was calculated using

$$t = \frac{x_{test} - x_{ref}}{\sqrt{{\delta x_{test}}^2 + {\delta x_{ref}}^2}}, \tag{2.5}$$

where x_{test} and x_{ref} are the test and reference occupancy values respectively, and δx_{test} and δx_{ref} are the errors in these values. A histogram of t-values was then produced and fit to a Gaussian, from which a σ value was obtained. The t-values were then averaged over boards and compared to thresholds, which depend on the σ from the fit. The resulting plots for this stack-by-stack analysis are shown in Fig. 2.7.

The information for each stack was used to obtain the summary plot shown in Fig. 2.8. This figure shows a slice of the TRT detector, subdivided into boards. The boards were colored according to their average t-value, which gives an idea of how differently they are performing compared to the reference. A board was colored green if $|t_{avg}| < 1.5\sigma$, where t_{avg} is the average t-value for that board and σ is from the Gaussian fit. A yellow coloring corresponds to $1.5\sigma \leq |t_{avg}| < 2\sigma$, whereas a red coloring was obtained for $|t_{avg}| \geq 2\sigma$. In addition, in order to catch malfunctioning chips, boards containing at least one chip with $|t| > 5\sigma$ were flagged by a darker color. Finally, an entire stack was colored gray if the scaling factor between reference and test plots had a percent difference greater than 10% from the average scaling factor over all stacks. This was meant to identify stacks with a very unusual occupancy level, at which point the board coloring is no longer relevant. This figure allows one to quickly locate areas which need

[a] ATLAS uses a right-handed coordinate system with the nominal collision point at the origin. The anti-clockwise beam direction defines the positive z-axis, the positive x-axis is defined as pointing from the collision point to the center of the LHC ring and the positive y-axis points upwards. The azimuthal angle, ϕ, is measured around the beam axis, in the x-y plane.

special attention and then return to the stack analysis, as in Fig. 2.7, to further investigate the cause of the anomaly.

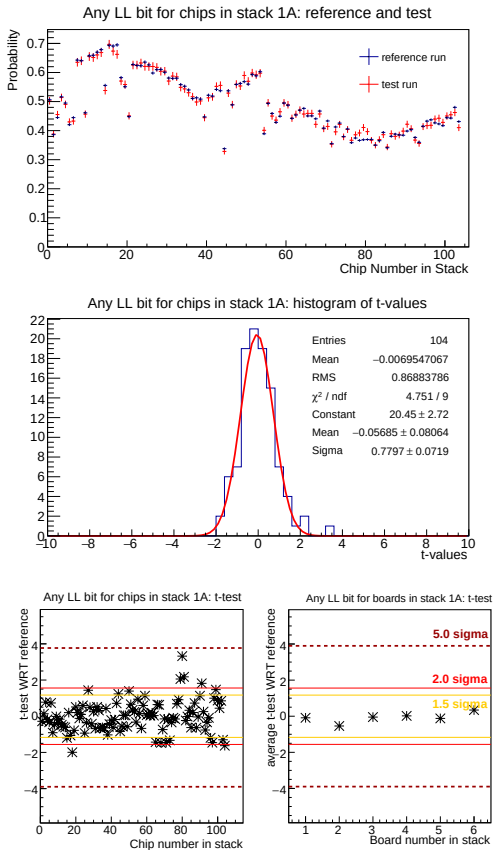

Figure 2.7: Example of single stack analysis for a particular plot (LT occupancy for chips) in stack 1 for run 331033. The upper figure shows the reference and test plots overlapped. The middle figure shows a histogram of t-values, fit to a Gaussian. The lower plots show t-values by chip and board number, along with the thresholds for coloring the boards as seen in Fig. 2.8.

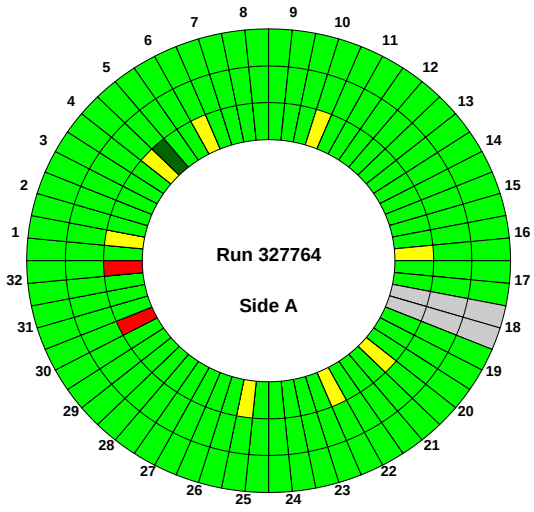

Figure 2.8: Example of a visual summary plot for run 327764. The figure shows a slice of the TRT detector, subdivided into boards. The stack numbers are found at the stack midpoint. Boards are colored according to their average t-value. A darker color board is a flag for outlier chips and a gray stack indicates an unusual occupancy level. Note that a threshold of 1% difference with the average scaling factor was used for this last feature instead of the nominal 10% in order to display all possible warnings on one plot.

This process was applied to multiple runs, immediately after data collection. No significant problems were detected and our results generally agreed well with existing monitoring systems. The thresholds for coloring were continually being fine-tuned to avoid too many false alarms without missing possible problems. Some interesting observations were made such as a larger number of warnings in the inner layers, as well as some consistently noisy chips across multiple runs. This proves that the described procedure indeed aids data monitoring by providing a quick way to narrow down the location and cause of a possible abnormality.

[Han09] M. Hance *et al.*, ATLAS Note, (2009).

[Kli08] E. Klinkby, Ph.D. thesis, University of Copenhagen, 2008.

2.4 Testing the Performance of Electron Identification in the Transition Radiation Tracker at the ATLAS Experiment

E. Le Boulicaut, *Gustavus Adolphus College, Saint Peter, MN*; M. Kruse, D. Davis, *Duke University*

The Transition Radiation Tracker (TRT) is a part of the ATLAS detector which uses ionization in gas tubes to obtain tracking and particle identification information. A new method for electron identification in the TRT using Time over Threshold (ToT) information is currently being investigated. In order to advance this study, the performance of a new calibration for the ToT algorithm was assessed and compared to an older version. Preliminary results show only a very slight improvement in efficiency. Enhanced performance is nevertheless expected in the future and could aid in event reconstruction in the ATLAS detector as a whole.

The Transition Radiation Tracker (TRT) is part of the inner detector at the ATLAS Experiment. It contains a total of 298,000 gas-filled straw tubes providing tracking and particle identification information [Kit07].

When a particle passes through a straw, it ionizes the gas, thus releasing electrons which then travel to a wire in the center of the straw. This produces a signal which exceeds a Low Threshold (LT) and this information is used for tracking. However, it is also possible for the tracked particle to emit an X-ray photon as it passes through the layers of the material between the straws. This photon is absorbed by the gas, which again leads to the release of an electron. The signal received in this case is much larger and exceeds a High Threshold (HT). This is called transition radiation and occurs almost exclusively for electrons [Kli08], thus providing particle identification information, which is then validated by other ATLAS sub-detectors. However, the Time over the low Threshold (ToT) is also affected by transition radiation and could be an additional and independent way of identifying electrons.

The goal of this work was to test a new calibration of the ToT particle identification algorithm and compare it to the original version, which is currently outdated and unused.

The method for testing this particle identification tool depends on a variable called eProbToT, which expresses the probability of a particle being identified as an electron using ToT information. The algorithm used to calculate this variable contains a set of parameters which depend on detector material and are obtained from a calibration. In order to assess the effectiveness of both the original and new calibrations, two data samples were used: one containing only electrons (from $J/\psi \rightarrow ee$) and one containing only muons (from $J/\psi \rightarrow \mu\mu$). The histograms of the quantity eProbToT were obtained for both samples and were found to have a lot of overlap, which is an indication of poor performance. In order to quantify the amount of overlap between the histograms, a ROC (receiving operator characteristic) curve was obtained. It shows the muon efficiency as a function of electron efficiency, as seen in Fig. 2.9. This gives an idea of how many muons are falsely identified as electrons for a given fraction of correctly identified electrons. The curve should have the highest possible curvature, which is not the case here, indicating that the ToT tool discriminates poorly between electrons and muons. It can also be seen in Fig. 2.9 that the result for the new calibration was almost identical to the original, which means the performance is not significantly enhanced.

In order to study the correlation between the performance of the tool and the area of the detector, a plot of efficiency as a function of η (pseudorapidity) [a] was obtained and is shown in Fig. 2.10. Each point corresponds to the muon efficiency for 90% electron efficiency from a single ROC curve for a given η slice. For both the original and the new calibrations, the performance is better around $\eta = 0$, as can be seen from the dip in false identifications. However, it is once again clear that no significant improvement is

[a] ATLAS uses a right-handed coordinate system with the nominal collision point at the origin. The anti-clockwise beam direction defines the positive z-axis, the positive x-axis is defined as pointing from the collision point to the center of the LHC ring and the positive y-axis points upwards. The polar angle, θ, is the angle measured with respect to the z-axis. The pseudorapidity is given by $\eta = -\ln\tan(\theta/2)$.

observable between the two calibrations.

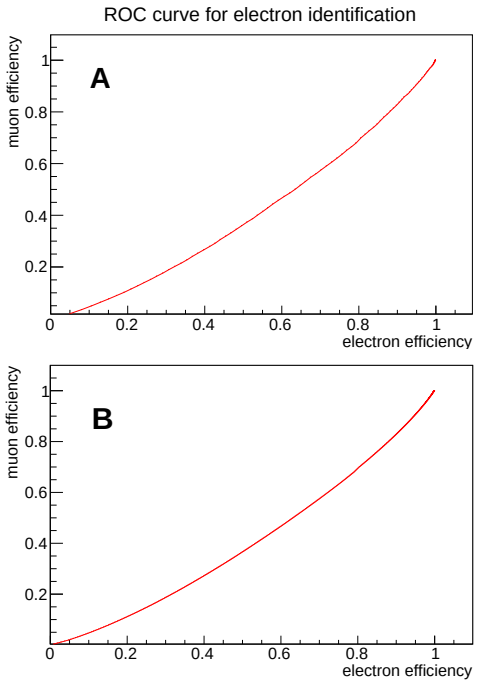

Figure 2.9: ROC curves for electron identification using Time over Threshold information. Figure A corresponds to the original calibration and Figure B to the new calibration. No significant improvement is observed between the two.

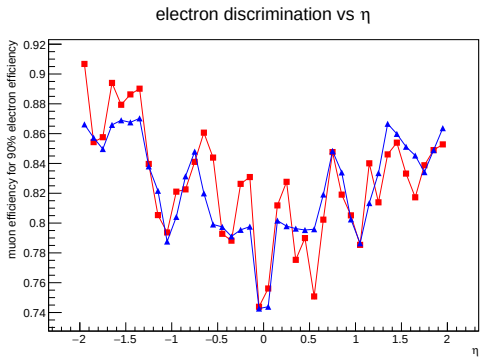

Figure 2.10: Fraction of muons falsely identified as electrons for 90% of correctly identified electrons using Time over Threshold, for different η slices. Square markers represent the original calibration, while triangles are for the new calibration. No significant improvement is observed between the two calibrations.

Additional calibrations are currently being developed and will hopefully produce better results. A comparison can then be made between the ToT and HT methods, and a new algorithm combining both methods could be created in order to improve the overall performance of particle identification in the TRT.

[Kit07] T. Kittelmann, Ph.D. thesis, University of Copenhagen, 2007.

[Kli08] E. Klinkby, Ph.D. thesis, University of Copenhagen, 2008.

2.5 Optimizing the Number Neural Networks in the ATLAS Pixel Detector for the High-Luminosity LHC Upgrade

R. Xu, *Carnegie Mellon, Pittsburgh PA*; A.V. Kotwal, *Duke, Durham NC*

In the High-Luminosity LHC upgrade, the ATLAS pixel detectors will be replaced. The replacements will likely have decreased digital resolution to satisfy bandwidth limitations. The pixel detector neural networks, used in track reconstruction, will need to be retrained. However, the dependence of network efficiency on the training configuration needs to be determined. This dependence for the number neural network has been examined by training several networks with varying training configurations, using simulated dijet events and detector responses. An optimal training configuration has been determined, as well as a suitable saturation point for the pixel sensors.

The pixel detectors are the inner-most layers of the ATLAS detector. Each pixel measures the charge deposited by ionizing radiation via a time-over-threshold (ToT) method, in 8 bits [Aad08]. When a particle interacts with the pixel detector, it will usually trigger many neighboring pixels, termed a pixel *cluster*. In high-density environments, clusters from different particles will frequently overlap, forming one large cluster. ATLAS uses a number neural network (number NN) to determine probabilities that a cluster contains 1, 2, or 3+ particles.

With the High-Luminosity LHC upgrade, the pixel detectors will be replaced. Bandwidth limitations will likely require the replacement to measure ToT in 4 bits. The different resolution and geometry will require retraining the NN. It is thus necessary to examine the relationship between training configuration and NN efficiency, so that the most efficient network can be produced when the upgrade arrives.

There are three key hyperparameters involved in the training of a NN:
1) **Learning Rate**: How fast the network will change its weights at every step (default 0.08)
2) **Momentum**: Use a fraction of the previous step in the current step (default 0.4)
3) **Regularizer**: Applies penalties for excessively large weights (default 1e-7)

To determine the dependence of NN efficiency on these parameters, several networks were trained with varying hyperparameters, and their performance evaluated. The trainings used simulated dijet events from the PYTHIA Monte Carlo generator [Sjo06], interfaced with a GEANT4 simulation of the ATLAS detector [ATL10], totaling one million clusters. The simulation uses the current pixel detector architecture, which measures ToT in 8 bits. To convert to 4 bits, we introduce a simulated saturation point x, which is also varied. The conversion is performed by

$$ToT_{4bit} = \begin{cases} int\left(ToT_{8bit} \times \frac{16}{x}\right) & ToT_{8bit} < x \\ 15 & ToT_{8bit} \geq x \end{cases} .$$

Alongside adjusting hyperparameters and the saturation point, a cross-validation (CV) scheme was introduced. The current NN reserves a fixed 10% of its training set as a validation set; training is stopped when the loss against the validation set stops decreasing for 20 epochs. In k-fold CV, the training set is split into k equal parts. Then k networks are trained, where the ith network uses the ith part for its validation set, and the remaining data for its training. To obtain a probability, one simply averages the outputs of the k individual networks. A hyperparameter analysis was also conducted using 4-fold CV.

To analyze the efficiency of the NNs, each NN was evaluated on 100,000 simulated clusters, disjoint from the training set. The Mann-Whitney U statistic [Man47] is then used to quantify how effective each network is. This analysis results in six U values; we denote the comparison MvsN as comparing M-particle and N-particle clusters, ranking with the NN's probability for a M-particle cluster. Each value is normalized against its maximum possible value, so that $U = 0.0$ indicates perfect NN efficiency and $U = 0.5$ would be the expected value obtained from random guessing.

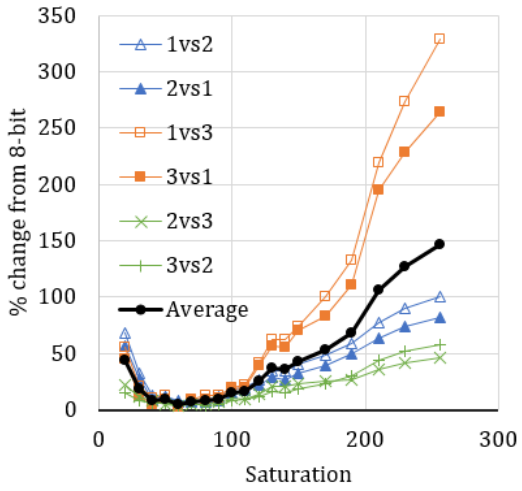

Figure 2.11: U values from varying the saturation point, as percent changes from values using a NN trained on 8-bit data. Hyperparameters were left at default settings, with no cross-validation.

The dependence of the U values on the saturation point are shown in Fig. 2.11. The six U values and their average are plotted as percent changes from the corresponding values using a NN trained on the original 8-bit data. These trials had no CV, and used the default hyperparameters. A clear minimum appears at a saturation point of $x = 60$, where the performance is only around 5% worse than that at full 8-bit resolution.

The effect of introducing CV is shown in Fig. 2.12. Because the training algorithm utilizes random numbers when initializing a network's weights, there exists some variance between different networks trained with the same configuration. These correspond to a standard deviation in the U values of around 1%. Fig. 2.12 plots the change in the U statistics using k-fold CV from the U values without CV, divided by the uncertainty from randomness (Δ/σ). Negative Δ/σ indicates an improvement in performance. A significant improvement is seen by introducing CV, with k=6 folds producing the best results.

Finally, the dependence of the U statistic on the three hyperparameters is shown in Table 2.2. Here, the changes in the U statistics by altering a single hyperparameter are divided by the uncertainty from randomness (Δ/σ). The values displayed are an average of the individual Δ/σ for the six U comparisons, with $x = 90$ saturation. The analysis was conducted for both no CV and 4-fold CV. Notably, the effect of changing a single hyperparameter is often within 1σ, and the only improvement with $\Delta/\sigma < -1$ is learning rate = 0.04 using 4-fold CV. This suggests the default hyperparameter settings are fairly robust and optimized already.

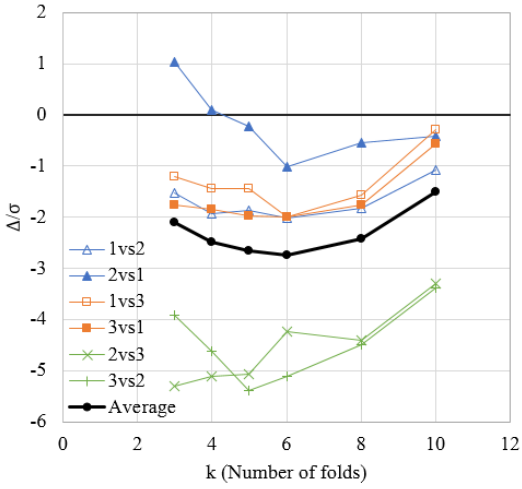

Figure 2.12: $\Delta U/\sigma$ from k-fold cross-validation, compared to no cross-validation, at saturation $x = 90$.

Table 2.2: $\Delta U/\sigma$ from varying a single hyperparameter at saturation $x = 90$. The tests used both no CV and 4-fold CV, with Δ/σ calculated from the respective default configuration. Results are an average over the 6 U values.

Hyperparameter Setting		No CV	4-fold CV
Momentum (default = 0.4)	0.2	-0.44	-0.44
	0.6	0.73	0.99
	0.8	1.72	3.07
Learning Rate (default = 0.08)	0.04	-0.61	-1.13
	0.12	0.41	-0.02
	0.16	0.77	1.56
Regularizer (default = 1E-07)	2E-07	-0.18	0.42
	1E-06	-0.23	1.64
	1E-05	1.04	11.67

[Aad08] G. Aad *et al.*, JINST, **3**, 1 (2008).

[ATL10] ATLAS Collaboration, Eur. Phys. J. C, **70**, 823 (2010).

[Man47] H. B. Mann and D. R. Whitney, Ann. Math. Stat., **18**, 50 (1947).

[Sjo06] T. Sjstrand, S. Mrenna, and P. Skands, JHEP, **5**, 26 (2006).


The Harris Team
welcomes you


Accelerating Science
CERN
w.cern.ch


HAVEN

Index